On the Effects of Anisotropic Turbulence on Leading Edge Noise

Fernando Gea-Aguilera[1], Ravish Karve[1], James Gill[1], Xin Zhang[2], and David Angland[1]

[1]Airbus Noise Technology Centre, University of Southampton, UK
[2]The Hong Kong University of Science and Technology, Hong Kong SAR

Author Accepted Manuscript

This is the Author Accepted Manuscript of:

Gea-Aguilera, F., Karve, R., Gill, J., Zhang, X., & Angland, D. (2021). *On the effects of anisotropic turbulence on leading edge noise.* Journal of Sound and Vibration, 495, 115895.

DOI: https://doi.org/10.1016/j.jsv.2020.115895

This manuscript has been accepted for publication but has not been copy-edited or typeset. The final Version of Record is available at the DOI above.

Abstract

This paper presents an investigation on the broadband noise produced by the interaction of anisotropic turbulence with isolated aerofoils. Computational aeroacoustic simulations are performed using a synthetic turbulence method with a linearised Euler solver. A comprehensive and fundamental parameter study on leading edge noise is presented to assess the effects of aerofoil thickness, mean flow Mach number, and angle of attack in the presence of moderately anisotropic turbulence. To this end, the streamwise-to-transverse length scale ratio is varied from 0.33 to 3, which can be representative of the anisotropy in the fan wakes from aero-engines, grid-generated turbulence in open-jet wind tunnel experiments, and rotors ingesting turbulent boundary layers. Anisotropic turbulence presents a significant redistribution of the energy in the turbulence spectra in comparison with an isotropic baseline, which affects the resulting noise spectra. It has been found that the noise spectra are mainly influenced by the transverse velocity component for the examined anisotropic flows. The frequency at which the noise spectrum is at a maximum only relies on the mean flow speed and the axial length scale of the anisotropic turbulent flow. Noise reduction due to aerofoil thickness at high frequencies follows a linear trend, but the amount of noise reduction is sensitive to the anisotropy in the flow. It is shown that the contribution of the streamwise disturbances and length scale become increasingly important for thick aerofoils at high Mach numbers and for aerofoils at non-zero angle of attack.

1 Introduction

Leading edge noise, which is also known as turbulence-aerofoil interaction noise, has been extensively investigated from analytical [1,2], numerical [3–5] and experimental [6–8] perspectives,

assuming isotropic turbulence. Thus, the effects of aerofoil thickness, angle of attack and camber are well documented. An increase in the aerofoil thickness and nose radius leads to a noise reduction at high frequencies [3–6,8]. However, variations in angle of attack and camber have a reduced impact on the leading edge noise from aerofoils interacting with isotropic turbulence [3,7]. To date, few works have studied the effects of anisotropic turbulence on leading edge noise, which may be a relevant subject for aero-engine noise. For conventional turbofan engines, anisotropic turbulence can be found at the fan intake [9,10], fan wakes [11,12], and boundary layers interacting with the fan tip. For installed contra-rotating open rotors and boundary layer ingesting propulsion systems, rotor blades interact with the boundary layer developed on the aircraft fuselage, which may present highly anisotropic turbulence [13]. Atmospheric turbulence ingested by helicopter rotors also presents a certain degree of anisotropy [14].

In the current generation of commercial aircraft, broadband noise from turbofan engines is a major source of noise during take-off and landing [15]. The dominant mechanism of fan broadband noise is associated with the interaction between the fan wakes and the Outlet Guide Vanes (OGVs), as shown by Ganz et al. [16]. Anisotropic turbulence has been reported experimentally in hot-wire measurements from fan wakes. For example, Podboy et al. [11] found a streamwise-to-transverse integral length scale ratio, $L_{11}^{(1)}/L_{22}^{(1)}$, that varies between approximately 1.2 and 3.5 depending on the radial location, whereas $L_{11}^{(1)}/L_{22}^{(1)} = 2$ is expected for isotropic turbulence [17]. Jenkins [12] found that the averaged ratios $L_{11}^{(1)}/L_{22}^{(2)}$ and $L_{22}^{(2)}/L_{33}^{(3)}$ along the span were 0.9 and 0.6, respectively. These ratios are unity for isotropic turbulence. Anisotropic turbulent flows are also encountered in other parts of the engine that contribute to broadband noise emissions. In static test conditions, variations of the order of 10^2 between streamwise and transverse length scales were reported at the fan intake by Hanson [9] without using a Turbulence Control Structure (TCS). Although the level of anisotropy is notably reduced when using a TCS to reproduce in-flight conditions [10,18], the ratio of streamwise-to-transverse length scales remains important. In experimental tests of turbulent boundary layer ingestion, reported values of $L_{11}^{(1)}/L_{22}^{(2)}$ vary between 2 close to the rotor tip and 6 close to the rotor hub [13].

Previous works in the field suggest that anisotropic turbulence at the fan intake [18], fan wakes [11] and boundary layers interacting with rotor blades [13,19] can be modelled as axisymmetric turbulence. This type of turbulence corresponds to a simple representation of an anisotropic flow, in which the root-mean-square velocity and length scale vary in a prevailing direction [20], such as the engine axis. Atassi and Logue [21] used an axisymmetric turbulence model that is based on rapid distortion theory [22] to study turbulence ingestion noise from the fan intake. For turbulence that is stretched in the axial direction, it was found that the maximum noise level moved to lower frequencies, followed by a decrease in noise in the mid-frequency range. A different turbulence modelling was used by Hanson [23] and Posson et al. [24] in analytical flat plate cascade models, who employed the homogeneous axisymmetric turbulence model of Kerschen and Gliebe [18]. This model corresponds to a modified Liepmann spectrum to account for variations in axial and lateral turbulence statistics. For turbulence that is stretched in the axial direction, Posson et al. [24] found the acoustic power spectra to be highly sensitive to the input turbulence spectra through a comparison between isotropic and

anisotropic turbulence. For example, it has been reported that turbulence stretched in the axial direction can lead to noise variations of up to 16 dB at high frequencies, and shifts the maximum noise level towards lower frequencies, which is consistent with the observations of Atassi and Logue [21]. The axisymmetric turbulence model of Kerschen and Gliebe [18] has recently been adopted by Karve et al. [13] to study the noise produced by a boundary layer interacting with a rotor. Paterson and Amiet [14] studied the noise radiated by a scaled helicopter rotor ingesting grid-generated and atmospheric turbulence. The experimental measurements were compared with predictions from Amiet's simplified rotational model. They modelled the anisotropy in the turbulence using a modified von Kármán spectrum. It was shown that the isotropic turbulence model produced discrepancies of up to 25 dB while the anisotropic turbulence model produced predictions that were within 5 dB of the measurements.

Based on the observations discussed above, it can be inferred that analytical models for the prediction of broadband noise from rotor blades and stator vanes interacting with anisotropic turbulence are highly sensitive to the input turbulence spectrum [13,14,23,24]. Therefore, the effects of anisotropic turbulence should be studied on simplified configurations, such as isolated aerofoils, to improve current understanding.

There are few experimental studies that are intended for anisotropic turbulence-aerofoil interaction noise, although grid-generated turbulence in wind tunnel facilities normally presents a certain level of anisotropy. For example, Paterson and Amiet [6] reported a $L_{11}^{(1)}/L_{22}^{(1)}$ ratio of 1.25. Unlike the majority of experiments on turbulence-aerofoil interaction noise, which use grid-generated turbulence, Olsen and Wagner [25] tested a number of thick symmetrical aerofoils at zero angle of attack interacting with a jet shear layer, where anisotropy is more pronounced. The study showed a significant reduction in noise levels at high frequencies, which is consistent with findings in experiments using nearly isotropic turbulence (for example, see Refs. [6,8]). Hall et al. [26] measured the noise from thick aerofoils with various leading edge geometries interacting with anisotropic turbulence from a boundary layer. The scaling law of Gershfeld [27] to predict aerofoil thickness effect on noise showed an acceptable agreement with experimental results, despite the fact that the scaling law was applied by assuming isotropic turbulence. Devenport et al. [28] assessed the angle of attack effect on leading edge noise due to anisotropic turbulence by means of a panel method [29]. This study was performed on a NACA 0015 aerofoil by using the axisymmetric turbulence spectra proposed by Kerschen and Gliebe [18]. Devenport et al. [28] reported a significant increase in noise levels with increasing angle of attack for turbulence stretched in the axial direction. However, the study was limited to low frequencies and incompressible Mach numbers. To overcome these limitations, Gea-Aguilera et al. [30] performed leading edge noise predictions from isolated aerofoils at moderate Mach numbers using anisotropic synthetic turbulence and a Computational AeroAcoustic (CAA) solver. Initial results showed that noise reduction due to aerofoil thickness follows similar trends for both isotropic and moderately anisotropic turbulent flows, and variations in angle of attack might have a limited impact. Recently, Zhong and Zhang [31] and Shen and Zhang [32] have studied the effect of the streamwise velocity fluctuations on leading edge noise from isolated aerofoils at zero angle of attack using CAA simulations. Although these studies were limited to small variations in lateral length scales, it was found that the contribution of the streamwise component to the

noise levels can be relevant in the upstream direction at high Mach numbers.

The motivation of this work is to present an extensive investigation on the effects of moderately anisotropic turbulence on leading edge noise. To this end, anisotropic synthetic turbulence is combined with a Linearised Euler Equation (LEE) solver to model the turbulence-aerofoil interaction noise. To reduce the computational expense, two-dimensional CAA simulations are performed by using anisotropic synthetic turbulence with the key statistics of the homogeneous axisymmetric model of Kerschen and Gliebe [18]. Variations of streamwise-to-transverse length scales ranging from 0.33 to 3 are considered for the anisotropic turbulent flows. Far-field noise predictions have been obtained from the two-dimensional aerofoil response using a three-dimensional Ffowcs Williams and Hawkings (FW-H) solver. This approach, which is able to capture the main physics of turbulence-aerofoil interaction [5,32,38], has been used to investigate noise variations due to anisotropy from a number of isolated aerofoil configurations with straight leading edge, including variations in freestream Mach number, aerofoil thickness, and angle of attack. This paper is organised as follows. Section 2 presents the CAA solver that has been used in this work. In Section 3, a synthetic turbulence method is presented and validated to reproduce the homogeneous axisymmetric spectra of Kerschen and Gliebe [18] from the superposition of anisotropic Gaussian spectra with various length scales. Section 4 presents the computational setup of the CAA simulations. A detailed parameter study and discussion on the effects of anisotropic turbulence on leading edge noise is presented in Section 5. Finally, the main findings are summarised in Section 6.

2 CAA Solver

In the current work, a high-order accurate finite difference CAA solver has been used to perform all numerical simulations. This CAA solver has successfully been used in previous numerical studies of turbulence-aerofoil/cascade interaction noise [3,5,33]. The CAA code solves the LEEs in the time-domain by using a 4th-order implicit spatial scheme [34]. The numerical stability is preserved by filtering the numerical solution after each time step [35]. A 4–6 stage low dispersion and dissipation Runge-Kutta numerical method is used as the time marching scheme [36]. Implicit buffer zones [37] are used as a non-reflecting condition at the domain boundaries, and a slip-wall condition is applied on the aerofoil surface. All CAA simulations presented in the current work were performed at freestream density $\rho_0 = 1.2$ kg/m^3 and speed of sound $c_\infty = 340$ m/s. The reference values for the sound PoWer Level (PWL) and Sound Pressure Level (SPL) are $\mathcal{P}_{\text{ref}} = 1 \times 10^{-12}$ W and $p'_{\text{ref}} = 2 \times 10^{-5}$ Pa, respectively. The reference length and speed are $L_{\text{ref}} = 1$ m and $U_{\text{ref}} = 1$ m/s, respectively.

3 Anisotropic Synthetic Turbulence

Synthetic turbulence for CAA simulations of leading edge noise predictions can be generated through a summation of Fourier modes [3,38], synthetic eddies [39], or digital filters [5,40]. In this section, a digital filter method [5] is adapted to generate two-dimensional anisotropic synthetic turbulence with the key statistics of the homogeneous axisymmetric model of Kerschen

and Gliebe [18]. To this end, a number of anisotropic Gaussian spectra with various length scales are superimposed to reproduce a target velocity spectrum.

3.1 Generalised anisotropic turbulence from Gaussian superposition

The superposition of Gaussian-like spectra is common practice to expand the spectral content of synthetic turbulent flows, and has successfully been used in methods based on a summation of Fourier modes [41,42] and digital filters [5,43]. An advantage of using a superposition of Gaussian spectra is that it avoids the development and implementation of a specific set of equations for each type of turbulence spectrum to be reproduced.

In this work, two-dimensional synthetic turbulence with the statistics of a target velocity spectrum is generated by superimposing N_e anisotropic Gaussian velocity spectra, such that

$$\Phi_{ij}^{\text{sum}} = \sum_{n=1}^{N_e} \Phi_{ij,n}^{(2D)} \quad , \tag{1}$$

where Φ_{ij}^{sum} is the resulting velocity spectra and $\Phi_{ij,n}^{(2D)}$ corresponds to the nth two-dimensional Gaussian velocity spectra, which are given by

$$\Phi_{11}^{(2D)}(k_x, k_y) = \frac{2}{\pi^3} u_0'^2 l_x^2 l_y^2 k_y^2 \exp\left(-\frac{l_x^2 k_x^2}{\pi}\right) \exp\left(-\frac{l_y^2 k_y^2}{\pi}\right) \quad , \tag{2}$$

$$\Phi_{22}^{(2D)}(k_x, k_y) = \frac{2}{\pi^3} u_0'^2 l_x^2 l_y^2 k_x^2 \exp\left(-\frac{l_x^2 k_x^2}{\pi}\right) \exp\left(-\frac{l_y^2 k_y^2}{\pi}\right) \quad , \tag{3}$$

for streamwise and transverse disturbances, respectively. In Eqs. (2) and (3), (k_x, k_y) are the vortical wavenumber components and u_0' is a characteristic velocity term. The root-mean-square velocities are obtained through integration of the velocity spectra in Eqs. (2) and (3) over the whole range of wavenumbers, which leads to $u'_{x,\text{rms}} = u_0'\sqrt{l_x/l_y}$ and $u'_{y,\text{rms}} = u_0'\sqrt{l_y/l_x}$, respectively. To simplify the notation, the streamwise and transverse length scales are written here as $l_x = L_{11}^{(1)}$ and $l_y = L_{22}^{(2)}$, respectively. The $L_{ij}^{(m)}$ term corresponds to the integral length scale of the ith and jth fluctuating velocity components in the mth spatial direction, i.e.

$$L_{ij}^{(m)} = \int_0^\infty \frac{\langle u_i'(\mathbf{x} + r\mathbf{e}_m)\, u_j'(\mathbf{x})\rangle}{\langle u_i'(\mathbf{x})\, u_j'(\mathbf{x})\rangle}\, \mathrm{d}r \quad , \tag{4}$$

where u_i' represents the ith fluctuating velocity component, r is the separation between two points in the mth direction, $\mathbf{e}_m$ is a unit vector in the mth direction, and $\langle . \rangle$ is the ensemble average operator.

Synthetic turbulence with a target anisotropic turbulence spectrum can be obtained from the superposition of anisotropic Gaussian eddies, each of them being related to a given Gaussian spectrum. To this end, the governing equations of a two- dimensional isotropic Gaussian eddy (see Eqs. (11) and (12) in Ref. [5]) are extended here to account for spatial variations in length scales, taking advantage of the properties of the exponential function to vary the length of the filter in each spatial direction. Thus, the fluctuating velocity field generated by the summation of N_e anisotropic Gaussian eddies from the pth eddy centre is defined as

$$u'_{x,p}(\mathbf{x}) = -\sqrt{2\pi\,\Delta_{e,x}\Delta_{e,y}}\,(y-y_p)\sum_{n=1}^{N_e}\frac{\epsilon_{p,n}u'_{0,n}}{l_{y,n}^2}\exp\left[-\frac{\pi(x-x_p)^2}{2l_{x,n}^2}\right]\exp\left[-\frac{\pi(y-y_p)^2}{2l_{y,n}^2}\right] \quad , \quad (5)$$

$$u'_{y,p}(\mathbf{x}) = \sqrt{2\pi\,\Delta_{e,x}\Delta_{e,y}}\,(x-x_p)\sum_{n=1}^{N_e}\frac{\epsilon_{p,n}u'_{0,n}}{l_{x,n}^2}\exp\left[-\frac{\pi(x-x_p)^2}{2l_{x,n}^2}\right]\exp\left[-\frac{\pi(y-y_p)^2}{2l_{y,n}^2}\right] \quad , \quad (6)$$

where $\mathbf{x} = (x, y)$ is a point in the flow field, (x_p, y_p) corresponds to the pth eddy centre, $\epsilon_{p,n}$ is a random number that takes ± 1 and define the direction of rotation of the eddies, and $\Delta_{e,x}$ and $\Delta_{e,y}$ correspond to the separation between eddy centres along the injection plane. Each eddy introduces a divergence-free fluctuating velocity field around its centre ($\nabla \cdot \mathbf{u}' = 0$). It should be noted that the governing equations for isotropic Gaussian eddies are recovered by setting $l_{x,n} = l_{y,n}$ and $\Delta_{e,x} = \Delta_{e,y}$ in Eqs. (5) and (6).

Fig. 1 shows a schematic of the numerical implementation and contours of an anisotropic Gaussian eddy. Synthetic eddies are directly injected into the CAA domain through a local injection plane to generate anisotropic turbulence. Based on the limiting values presented by Gea-Aguilera et al. [5] for isotropic turbulence, the correct statistics of the anisotropic turbulent flow are recovered provided that the eddy spacing and the eddy radii satisfy

$$\Delta_{e,x} \leq \frac{\min\{l_{x,n}\}}{2}, \qquad \Delta_{e,y} \leq \frac{\min\{l_{y,n}\}}{2}, \qquad \text{for } n = 1, \ldots, N_e \quad , \quad (7)$$

$$r_{e,x} \geq \frac{3\,\max\{l_{x,n}\}}{2}, \qquad r_{e,y} \geq \frac{3\,\max\{l_{y,n}\}}{2}, \qquad \text{for } n = 1, \ldots, N_e \quad , \quad (8)$$

respectively. The eddy radii define the area of influence from each eddy centre in which the fluctuating velocity field needs to be computed. Since the eddies are convected as frozen turbulence by the mean flow, a new set of eddies is injected into the CAA domain every $\Delta_{e,x}/(U_\infty \Delta t)$ time steps, where Δt is the numerical time step of the simulation and U_∞ is the mean flow speed. The frozen turbulence assumption has been shown to be valid for leading edge noise predictions in the context of aero-engine broadband noise [44]. Nevertheless, synthetic turbulence that is injected into the CAA domain should have the statistics of the anisotropic turbulent flow near the aerofoil leading edge, as the return to isotropy is not modelled by the LEEs.

3.2 Homogeneous axisymmetric turbulence

For a turbulent flow with an axisymmetric axis that is aligned with the mean flow in the x-direction, the axial and transverse velocity spectra are defined according to Kerschen and Gliebe [18] as

$$\Phi_{11}(k_x, k_y, k_z) = \frac{2\,l_a\,l_t^4\,u_a'^2\left(k_y^2 + k_z^2\right)}{\pi^2\left[1 + l_a^2 k_x^2 + l_t^2\left(k_y^2 + k_z^2\right)\right]^3} \quad , \quad (9)$$

and

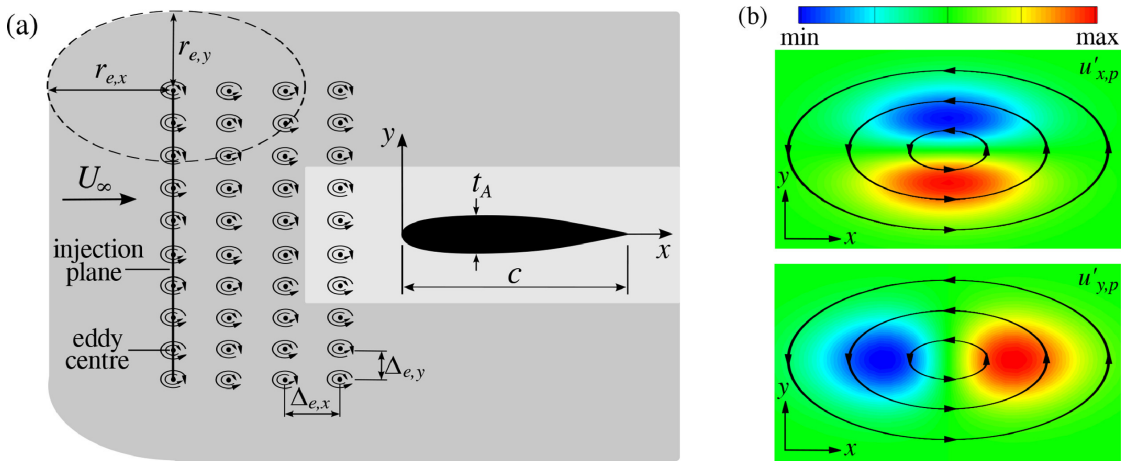

Figure 1: Computational setup to synthesise anisotropic turbulence. (a) Injection plane. (b) Example of fluctuating velocity contours and streamlines of a single anisotropic Gaussian eddy with $l_x = 3l_y$.

$$\Phi_{22}(k_x, k_y, k_z) = \frac{2\, l_a\, l_t^4\, u_a'^2}{\pi^2 \left[1 + l_a^2 k_x^2 + l_t^2 \left(k_y^2 + k_z^2\right)\right]^3} \left[k_x^2 + k_z^2 \left(2\frac{u_t'^2}{u_a'^2} - \frac{l_t^2}{l_a^2}\right)\right] \quad , \tag{10}$$

respectively, where l_a, u'_a and l_t, u'_t are the length scale and root-mean-square fluctuating velocity in the axial and transverse directions, respectively. The length scales in the model of Kerschen and Gliebe [18] are related to the integral length scales as follows

$$L_{11}^{(1)} = \frac{\pi}{u_a'^2} \int_{-\infty}^{\infty} \int_{-\infty}^{\infty} \Phi_{11}(k_x = 0, k_y, k_z) \mathrm{d}k_y \mathrm{d}k_z = l_a \; , L_{22}^{(2)} = L_{33}^{(3)} = l_t \quad , \tag{11}$$

$$L_{22}^{(1)} = \frac{\pi}{u_t'^2} \int_{-\infty}^{\infty} \int_{-\infty}^{\infty} \Phi_{22}(k_x = 0, k_y, k_z) \mathrm{d}k_y \mathrm{d}k_z = \frac{l_a}{2} \frac{u_a'^2}{u_t'^2} \left(2\frac{u_t'^2}{u_a'^2} - \frac{l_t^2}{l_a^2}\right) \quad . \tag{12}$$

It should be noted that the 'a' and 't' subscripts are preferred here for the turbulence length scales and root-mean-square fluctuating velocity to refer to the axial and transverse components, respectively, when using the homogeneous axisymmetric turbulence spectrum [18], instead of 'x' and 'y', which are reserved to the use of anisotropic Gaussian spectra in Section 3.1. The isotropic turbulence model proposed by Liepmann et al. [45] is recovered from Eqs. (9) and (10) by setting $u'_a = u'_t$ and $l_a = l_t$, which satisfy $L_{11}^{(1)}/L_{22}^{(1)} = 2$ as expected for isotropic turbulence.

For two-dimensional CAA simulations, synthetic turbulence with the key statistics of homogeneous axisymmetric turbulence is generated from a summation of N_e Gaussian spectra. To this end, Φ_{ij}^{sum} in Eq. (1) is set to reproduce the velocity spectra of homogeneous axisymmetric turbulence with $k_z = 0$ m^{-1}, where k_z corresponds to the spanwise wavenumber in this work. This assumption is based on the analytical flat plate model of Amiet [1], in which the spanwise wavenumber of the turbulence does not contribute to the broadband noise for an observer at the mid-span plane in the far-field. This result was proved to be valid if the turbulence length scales are small in comparison to the aerofoil span, which is satisfied in practical cases if the span-to-chord ratio is approximately $d/c \geq 3$ [38]. The $k_z = 0$ m^{-1} assumption has been used in previous CAA studies with different synthetic turbulence methods [3,5,32,38]. This type of tur-

bulence is often referred to as 'pseudo three-dimensional turbulence'. It should be noted that u'_t is not explicitly defined in Eqs. (9) and (10) if $k_z = 0$ m^{-1}. Nevertheless, u'_t is assumed to take a value that satisfies the constraint $2(u'_t/u'_a)^2 \geq (l_t/l_a)^2$, which ensures that the velocity spectra are positive when using the homogeneous and axisymmetric turbulence model of Kerschen and Gliebe [18].

Isotropic turbulence according to Liepmann et al. [45] is obtained by setting $l_a = l_t = 0.008$ m and $u'_a = 0.017U_\infty$. These values have been obtained from the Fundamental Case 1 of the Fan Broadband Noise Workshop organised at the AIAA aeroacoustics conference in 2014 [46]. From this baseline configuration, streamwise-to-transverse length scale ratios, l_a/l_t, are varied between 0.33 and 3 in this work. These values are representative of the anisotropic turbulence in the fan wakes from aero-engines [11,12] and grid-generated turbulence in open-jet wind tunnel tests [6]. Furthermore, these l_a/l_t values partially cover the anisotropy reported in dedicated experiments of boundary layers interacting with rotors [13]. The reader is referred to Appendix A for information on the specific values for $u'_{0,n}$, $l_{x,n}$ and $l_{y,n}$ that have been used to reproduce homogeneous axisymmetric turbulence spectra from the superposition of anisotropic Gaussian spectra.

To validate the synthetic turbulence approach, a monitor point has been placed within the CAA domain. The freestream Mach number, $M_\infty = U_\infty/c_\infty$, was set to 0.6, and 3×10^4 velocity samples were collected every 283 non-dimensional time steps, $c_\infty \Delta t/L_{\text{ref}} = 4 \times 10^{-6}$. The multitaper spectral analysis of Thomson [47] is used to calculate the numerical one- dimensional spectra from collected velocity samples over a frequency range from 80 Hz to 8080 Hz every 160 Hz. It should be noted that one-dimensional spectra for the fluctuating velocity can be obtained analytically from

$$E_{ij}(f, k_z = 0) = \frac{4\pi}{U_\infty} \int_{-\infty}^{\infty} \Phi_{ij}(k_x, k_y, k_z = 0) \mathrm{d}k_y \ , \tag{13}$$

where f is the frequency. Fig. 2 shows one-dimensional spectra of anisotropic turbulence for various degrees of anisotropy in the flow as a function of the chord-based Strouhal number, where the aerofoil chord, c, is set to 0.15 m in this work. Differences of less than 1.5 dB can be found between analytical and numerical turbulence spectra for most frequencies, showing the effectiveness of the anisotropic Gaussian superposition methodology.

Overall, the use of axisymmetric turbulence redistributes the energy of the velocity spectra in the wavenumber space, as shown in Fig. 3. The redistribution of the energy, which is caused by the different length scales involved, changes the amount of energy that could potentially contribute to the leading edge noise. This can be relevant for analytical models, which are quite sensitive to inflow turbulence data [24]. The implications of these observations on leading edge noise from isolated aerofoil configurations are discussed in Section 5.

4 Computational Setup for Leading Edge Noise Predictions

This section presents the CAA methodology and computational setup that have been used for the leading edge noise predictions. The isolated aerofoil configurations that are investigated in this study include a NACA 0001 aerofoil at zero angle of attack, $AoA = 0°$, and a NACA 0012

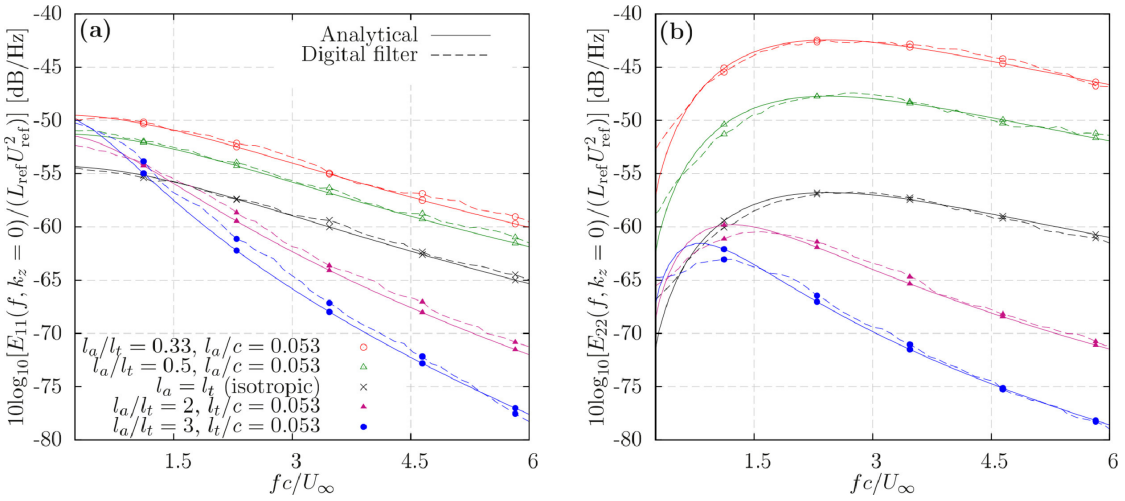

Figure 2: One-dimensional spectra of homogeneous axisymmetric turbulence. (a) Streamwise. (b) Transverse.

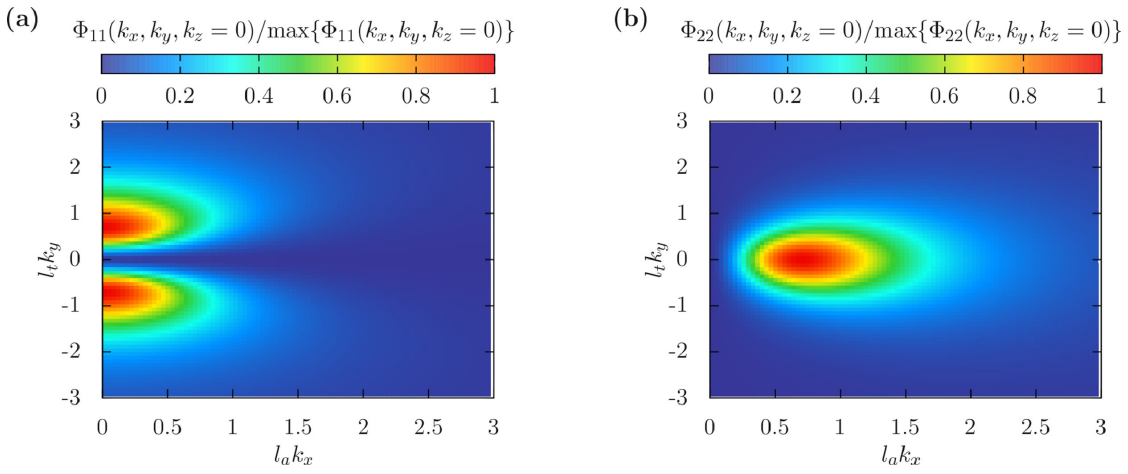

Figure 3: Normalised anisotropic velocity spectra in wavenumber space from Eqs. (9) and (10). (a) Streamwise. (b) Transverse.

aerofoil at $AoA = 0°$ and 6°. For NACA 4-digit aerofoils, the maximum aerofoil thickness, t_A, is given by the last 2 digits as a percent of the chord. For example, the maximum aerofoil thickness corresponds to $t_A = 0.12c$ for a NACA 0012 aerofoil. A low-cost CAA methodology has been adopted here to combine the two-dimensional aerofoil response from CAA simulations with a three-dimensional FW-H solver for the far-field noise propagation. This approach is similar to that proposed by Gea-Aguilera et al. [5]. Fig. 4 presents a schematic of the methodology steps.

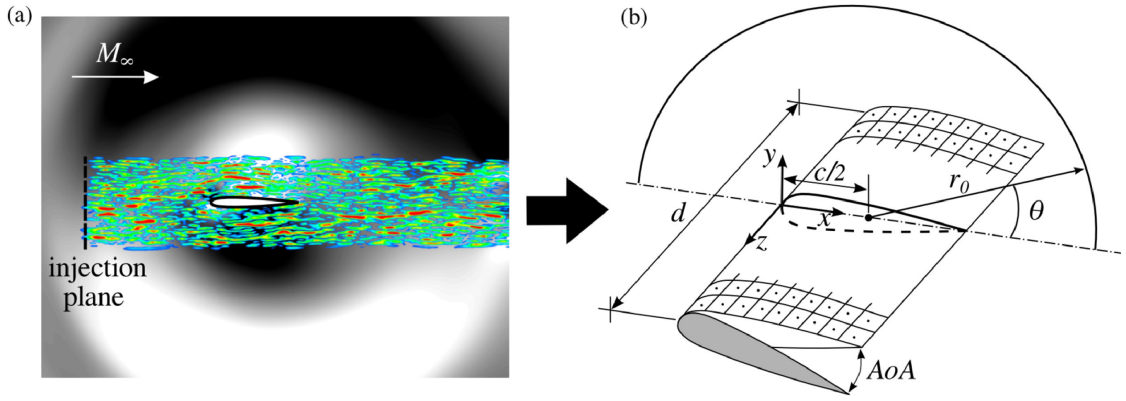

Figure 4: Schematic of the methodology steps. (a) Two-dimensional CAA simulation, where colour contours represent the vorticity field from anisotropic synthetic turbulence and grey contours represent the fluctuating pressure field. (b) Reference frame for three-dimensional far-field noise propagation.

Table 1: Order of magnitude of mesh design parameters in this work. Δ_{LE} corresponds to the cell size at the leading edge.

Aerofoil	AoA [°]	Grid points	Δ_{LE}/c	$c_\infty \Delta t / L_{\mathrm{ref}}$	$\max\{fc/U_\infty\}$
NACA 0001	0	318,890	7.0×10^{-5}	4×10^{-6}	6
NACA 0012	0	1,101,552	1.6×10^{-3}	8×10^{-5}	12
NACA 0012	6	1,425,214	1.1×10^{-3}	7.5×10^{-5}	12

Two-dimensional CAA simulations using three-dimensional homogeneous and anisotropic spectra with $k_z = 0$ m^{-1} are performed to compute the aerofoil response. Synthetic turbulence is introduced into the CAA domain through an injection plane that is located at least $r_{e,x}$ upstream of the aerofoil leading edge. Such a distance is required to allow for the convection and distortion of the synthetic turbulence before interacting with the aerofoil leading edge. The length of the injection plane has been set to approximately $2r_{e,y} + t_A$ at $AoA = 0°$.

In this work, the size of the CAA domain extends about $4c$ in all directions around the aerofoil centre, and the length of the buffer zone is set to $1c$ at the domain boundaries. The required grid resolution is at least 8 points-per-wavelength for the smallest vortical waves that are correctly propagated by the CAA code. Table 1 summarises the main characteristics of the CAA meshes, including information on the number of grid points, cell size at the leading edge, time step of the CAA simulations, and maximum frequency resolution. All structured grids were designed following the recommendations of Fattah et al. [48] for finite difference solvers. Fig. 5 shows details on the two-dimensional CAA mesh of a NACA 0012 aerofoil at $AoA = 6°$ that has been used in Section 5. On an indicative basis, the time per time step per grid point

of a two-dimensional CAA simulation using a NACA 0001 aerofoil is approximately 6×10^{-8} s on 128 processors. The mesh of the NACA 0001 aerofoil has 3.19×10^5 grid points and the CAA simulations were run for 8.5×10^6 time steps, such that the total time of each simulation was approximately 45h on 128 processors.

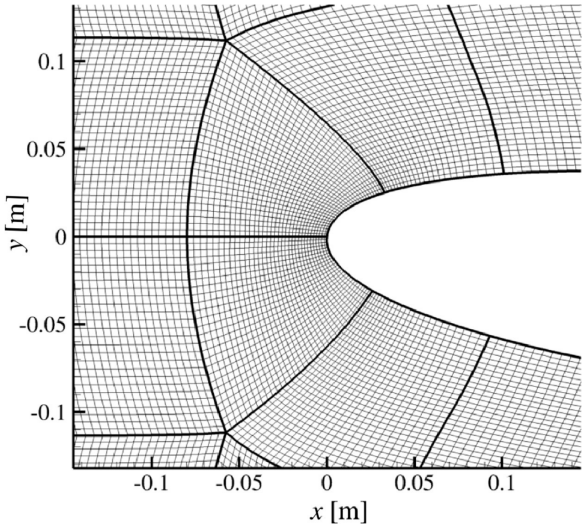

Figure 5: CAA mesh of a NACA 0012 aerofoil at $AoA = 6°$in the leading edge region.

Unsteady data are collected from at least 459 points that are distributed along the aerofoil surface from the two- dimensional CAA simulation. Then, unsteady data are copied 61 times along the aerofoil span, $d = 0.45$ m, to produce a three-dimensional aerofoil with straight leading edge that can be used as a solid surface in the FW-H solver. Thus, the span-to-chord ratio is set to $d/c = 3$, which is suitable for the $k_z = 0$ m^{-1} assumption, as discussed in Section 3.2. Another implication of the $k_z = 0$ m^{-1} assumption is that the CAA predictions do not consider any effects of spanwise correlation. The FW-H solver, which is based on the formulation 1A of Farassat and Succi [49], radiates the sound to the far-field in a uniform mean flow at a distance of $r_0 = 20c$ in the mid-span plane from the aerofoil semi-chord. Time-dependent pressure fluctuations are radiated from $\theta = 0°$ to $360°$ with an angle resolution of $1°$. The unsteady pressure in the far-field is used to compute the acoustic power by assuming cylindrical noise radiation [2],

$$\mathcal{P}(f) = \frac{dr_0}{2\rho_\infty c_\infty} \int_0^{2\pi} S_{pp}(r_0, \theta, f) \frac{\beta^4 A(\theta, M_\infty)}{[A(\theta, M_\infty) - M_\infty \cos\theta]^2} \mathrm{d}\theta \ , \tag{14}$$

where S_{pp} is the pressure spectral density, $\beta = \sqrt{1 - M_\infty^2}$, and $A(\theta, M_\infty) = \sqrt{1 - M_\infty^2 \sin^2\theta}$. The PWL spectrum is computed as $\mathrm{PWL}(f) = 10 \log(\mathcal{P}(f)/\mathcal{P}_{\mathrm{ref}})$.

5 Effects of Anisotropic Turbulence on Leading Edge Noise

This section presents a comprehensive study on the effects of moderately anisotropic turbulence on leading edge noise from isolated aerofoil configurations. Variations in freestream Mach number, aerofoil thickness, and angle of attack are examined in CAA simulations using the anisotropic turbulence spectra of Kerschen and Gliebe [18] for l_a/l_t varying between 0.33 and 3,

as discussed in Section 3.2. Table 2 presents a summary of the turbulence length scales for the various anisotropic turbulence cases in comparison with characteristic lengths of each aerofoil configuration, such as the aerofoil chord and thickness. It should be noted that turbulence length scales are small compared to the aerofoil chord in this work, where l_a/c and l_t/c can vary between 0.053 and 0.16 here. These values are consistent with available experimental data for fan wakes.

Table 2: Comparison of turbulence length scales for the various anisotropic turbulence cases.

l_a [m]	l_t [m]	l_a/l_t	l_a/c	l_t/c	l_t/l_a (NACA 0001)	l_t/l_a (NACA 0012)
0.024	0.008	3	0.16	0.053	5.3333	0.4444
0.016	0.008	2	0.107	0.053	5.3333	0.4444
0.008	0.008	1	0.053	0.053	5.3333	0.4444
0.008	0.016	0.5	0.053	0.107	10.6667	0.8889
0.008	0.024	0.33	0.053	0.16	16	1.3333

5.1 Flat plates and thin aerofoils at zero angle of attack

CAA simulations of a NACA 0001 aerofoil in a $M_\infty = 0.6$ flow at $AoA = 0°$ are presented here. The mean flow is assumed to be uniform in the CAA simulation, which is convenient for direct comparisons of noise results from the analytical flat plate model of Amiet [1]. Fig. 6 shows SPL and PWL spectra, where the flat plate results have been obtained from the analytical model of Amiet [1] by using the transverse velocity spectrum in Eq. (10). For further details on the flat plate model, the reader is referred to Appendix B.

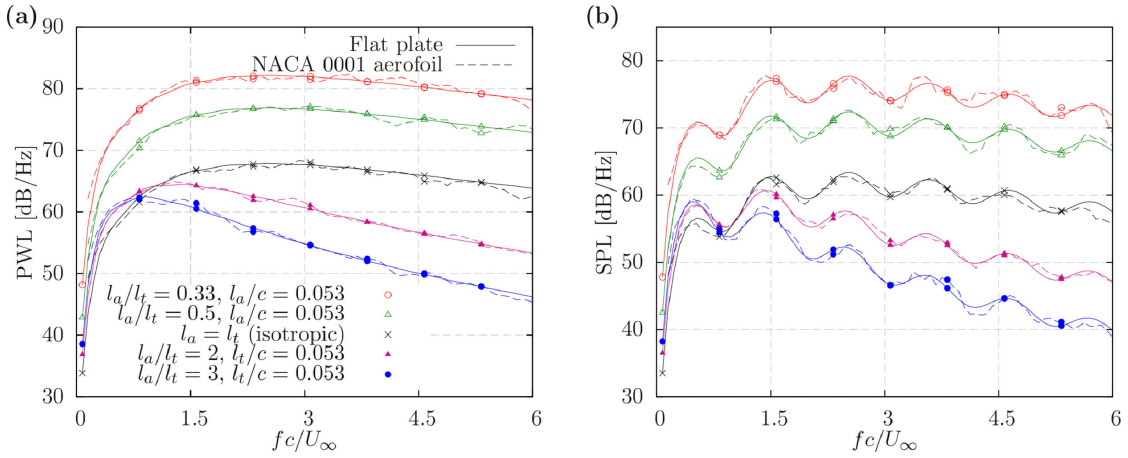

Figure 6: PWL and SPL spectra for a NACA 0001 aerofoil and a flat plate in anisotropic turbulence. (a) PWL spectra. (b) SPL spectra at $\theta = 90°$.

The agreement between numerical and analytical predictions is within 1.5 dB for most frequencies, which validates the current CAA methodology. Axisymmetric turbulence stretched in the streamwise direction with $l_a/l_t > 1$ produces a decrease in noise levels and a shift of the maximum noise amplitude towards lower frequencies in comparison with isotropic turbulence cases. This suggests that the effects of anisotropic turbulence on isolated flat plates and thin aerofoils are similar to those reported for cascade noise [21,24].

PWL spectra in Fig. 6 (a) closely follow the shape of the transverse velocity spectra in Fig. 2 (b), reaching the peak value at approximately the same chord-based Strouhal number for each anisotropic turbulence case. Thus, it can be inferred from Fig. 6 that leading edge noise due to the interaction of anisotropic turbulence with a thin aerofoil, $t_A/c = 0.01$, only depends on the transverse velocity spectrum. To further investigate the relationship between the transverse velocity and PWL spectra, Fig. 7 shows the effect of varying the turbulence length scales from the flat plate model of Amiet [1].

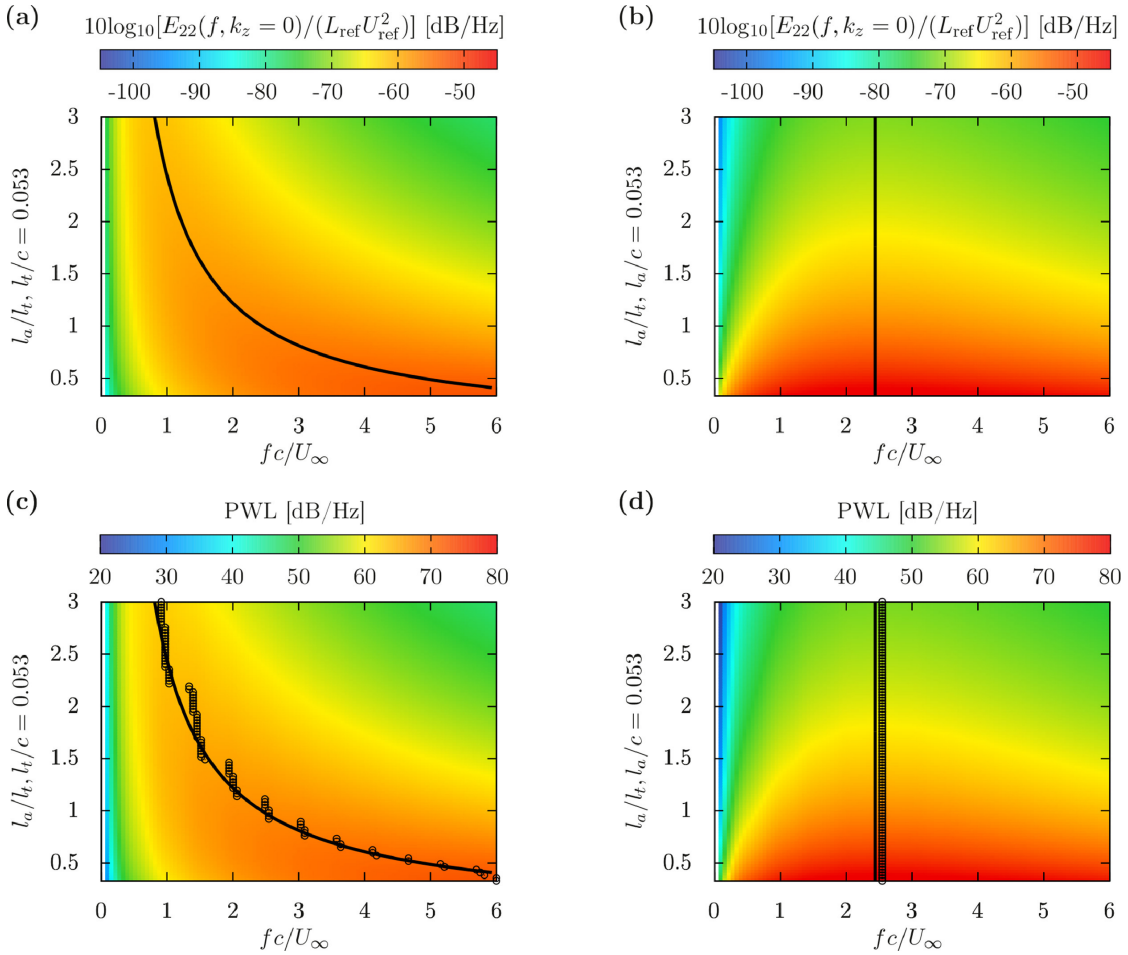

Figure 7: Analytical E_{22} and PWL spectra (using Amiet's theory [1]) for a flat plate for varying axial and transverse length scales. The black solid line and circles are a locus of the maxima of E_{22} and PWL, respectively. (a) E_{22} with l_a varying, (b) E_{22} with l_t varying, (c) PWL with l_a varying, (d) PWL with l_t varying.

Variations in the axial integral length scale have a twofold effect, as shown in Fig. 7 (a) and (c). Firstly, the frequency at which the maximum E_{22} occurs, decreases as the axial length scale is increased. Secondly, as l_a/l_t is increased with constant l_t, the amplitude of the spectra at low frequencies becomes relatively larger than at high frequencies. The first result can be explained from the one-dimensional spectrum of the transverse velocity fluctuations, which can be obtained analytically from Eqs. (10) and (13),

$$E_{22}(f, k_z = 0) = \frac{3\, l_t^3\, u_a'^2}{l_a\, U_\infty} \frac{l_a^2 k_x^2}{(1 + l_a^2 k_x^2)^{5/2}} \quad , \tag{15}$$

where $k_x = 2f/U_\infty$ from the frozen turbulence assumption. In Eq. (15), the $l_a k_x$ term can be seen as a scaling factor applied to the streamwise wavenumber and therefore, changing l_a can be thought of as elongating the eddies in the streamwise direction resulting in a subsequent redistribution of energy. However, the transverse length scale is only acting as a multiplicative constant and thus changing l_t would result in an increase in the amplitude of E_{22}. This is a consequence of setting the spanwise wavenumber k_z to zero. The frequency at which E_{22} from Eq. (15) is at a maximum can be written as,

$$f_{\max} = \sqrt{\frac{2}{3}} \frac{U_\infty}{2\pi l_a} \ , \tag{16}$$

which corresponds to $l_a k_x = \sqrt{2/3}$ in Fig.3 (b). These maximum frequencies are shown by black solid lines in the E_{22} and PWL spectra in Fig. 7. For a fixed mean flow speed, Eq. (16) implies that the E_{22} maxima will only change if the axial length scale is changed. This result is confirmed in Fig. 7 (b) and (d), where the frequencies at which the maximum in the transverse velocity and PWL spectra occurs does not change. The frequencies at which the PWL spectrum is at a maximum are shown by black circles in Fig. 7 (c) and (d). The aim of the black solid lines and the circles is to show that the maxima in PWL occur close to the maxima in the upwash velocity spectrum. Nevertheless, some discontinuities in the frequencies at which the PWL is at a maximum can be observed in Fig. 7 (c). These are related to the presence of small lobes in the PWL spectra, which are a consequence of the loss of compactness at high frequencies, and whose amplitudes change with varying l_a. From these figures, it can be inferred that Eq. (16) provides a good estimation of the frequencies at which broadband noise from anisotropic turbulence-aerofoil interaction could be dominant.

The maximum PWL for various length scales is shown in Fig. 8. It can be seen that the maximum PWL increases about 28 dB as the transverse length scale is increased from 0.0026 m ($l_t/c = 0.017$) to 0.024 m ($l_t/c = 0.16$) and decreases by approximately 10 dB as the axial length scale is increased from 0.0026 m to 0.024 m. From Eq. (15) it is also observed that the power should scale as $1/l_a$ for a constant transverse length scale and as l_t^3 for a constant axial length scale. These scaling laws are shown in Fig. 8. It should be noted that the maximum sound power deviates slightly from the $1/l_a$ trend for the larger length scales. This is likely due to the mean flow effects that are accounted for in Eq. (14). It should be noted that similar conclusions can be achieved by using a different anisotropic turbulence spectrum. For example, it can be shown that Eqs. (15) and (16) can be rewritten for the modified von Kármán spectrum proposed by Glegg and Walker [19] as,

$$E_{22}(f, k_z = 0) = \frac{16\, l_t^3\, u_a'^2}{9\, l_a\, U_\infty K_e^2} \frac{l_a^2 k_x^2 / K_e^2}{(1 + l_a^2 k_x^2 / K_e^2)^{7/3}}, \qquad f_{\max} = \sqrt{\frac{3}{\pi}} \frac{\Gamma(5/6)}{4\,\Gamma(1/3)} \frac{U_\infty}{l_a} \ , \tag{17}$$

respectively, where $K_e = [\sqrt{\pi}\Gamma(5/6)]/\Gamma(1/3)$, when assuming homogeneous axisymmetric turbulence with $k_z = 0$ m^{-1}.

For further validation of the CAA simulations, directivity patterns at $fc/U_\infty = 3$ and 6 are shown in Fig. 9. The agreement of the numerical results with the flat plate model of Amiet [1] is better than 2 dB at most observer angles. The location of the lobes due to the loss of

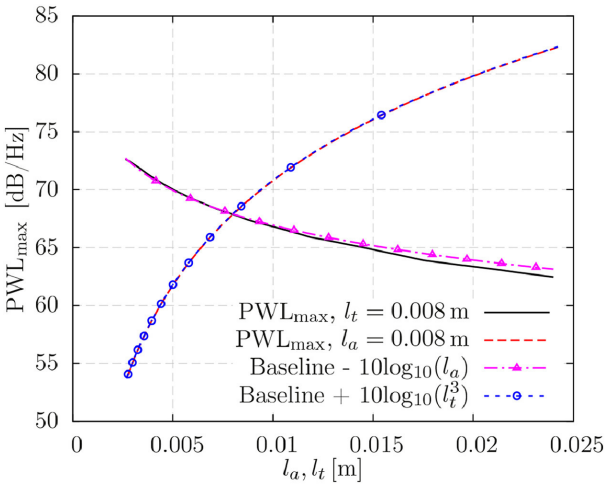

Figure 8: The maximum PWL at various axial and transverse length scales. The baseline for the scaling law corresponds to the maximum in PWL for isotropic turbulence with $l_a = l_t$.

compactness at high frequencies is correctly predicted by the numerical simulations.

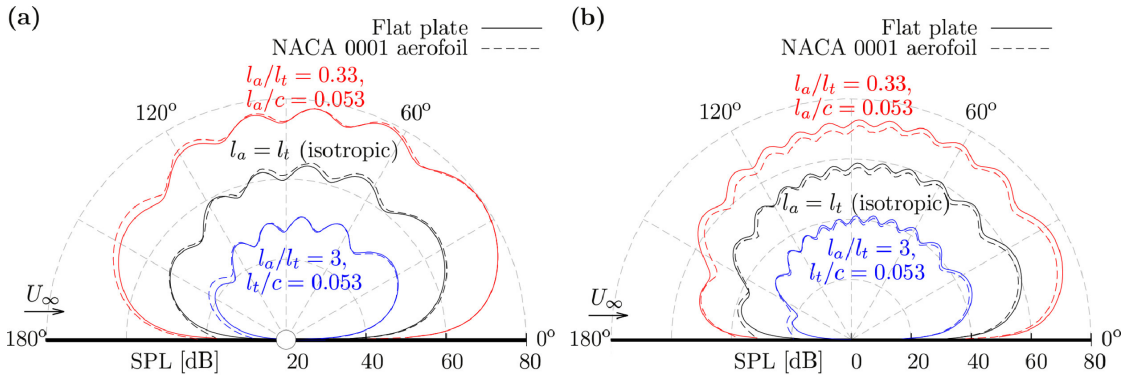

Figure 9: Directivity plots for a NACA 0001 aerofoil in anisotropic turbulence. (a) $fc/U_\infty = 3$. (b) $fc/U_\infty = 6$.

5.2 Thick aerofoils in a low-subsonic Mach number flow

The effects of anisotropic turbulence on leading edge noise from thick aerofoils are studied for a NACA 0012 aerofoil in a $M_\infty = 0.3$ flow at $AoA = 0°$. An inviscid mean flow was computed by using the Euler equations in a second-order finite volume CFD solver (FLUENT v14.5), and used as a background flow in the CAA simulation. It should be noted that the effect of mean flow viscosity was found to be negligible on leading edge noise [50], and can produce hydrodynamic instabilities near the trailing edge in CAA simulations [38], which are related to strong velocity gradients in the boundary layer region.

Fig. 10 shows instantaneous contours of non-dimensional vorticity magnitude and fluctuating pressure from CAA simulations with anisotropic turbulence stretched in the streamwise and transverse directions. In both cases, acoustic pressure is generated at the aerofoil leading edge and radiated to the far-field with a dipole-like directivity. However, pressure contours due to anisotropic turbulence with $l_a/l_t = 0.33$ present a broader frequency content than with $l_a/l_t = 3$. This observation is related to the spectral content of one-dimensional spectra in Fig.

2, in which the small amplitude difference between high and low frequencies in the $l_a/l_t = 0.33$ case results in a wide frequency content in the contours of fluctuating pressure. In contrast, most energy concentrates at low frequencies in one-dimensional spectra with $l_a/l_t = 3$.

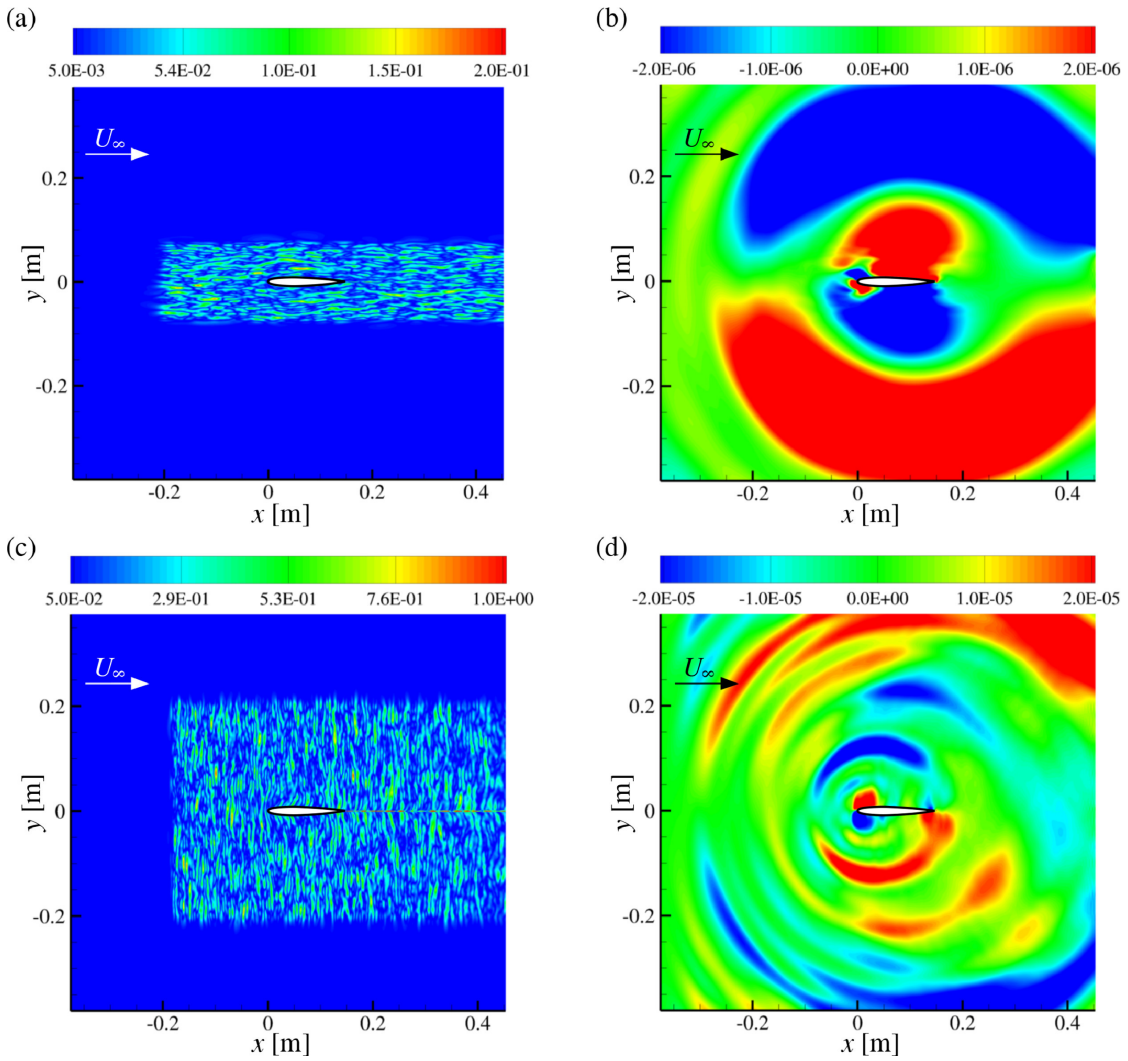

Figure 10: Instantaneous contour plots of a NACA 0012 aerofoil interacting with anisotropic synthetic turbulence at $M_\infty = 0.3$. A black solid line highlights the aerofoil surface. (a) Non-dimensional vorticity magnitude, $||\nabla \times \mathbf{u}'||L_{\text{ref}}/c_\infty$, with $l_a/l_t = 3$. (b) Non-dimensional fluctuating pressure, $p'/(\rho_\infty c_\infty^2)$, with $l_a/l_t = 3$. (c) Non-dimensional vorticity magnitude with $l_a/l_t = 0.33$. (d) Non-dimensional fluctuating pressure with $l_a/l_t = 0.33$.

Normalised values of root-mean-square fluctuating pressure, p'_{rms}, along the aerofoil chord are shown in Fig. 11. Overall, the aerofoil response presents a similar shape for the different degrees of anisotropy investigated. The maximum p'_{rms} is localised in the leading edge region, as expected when turbulence-aerofoil interaction is the dominant noise mechanism. However, some differences can be observed in the location of the maximum p'_{rms}, which moves towards the stagnation point at $x/c = 0$ as l_a/l_t increases. This suggests that the streamwise component of the fluctuating velocity field could become increasingly important for thick aerofoils.

Although the turbulence is convected as frozen turbulence upstream of the aerofoil, strong mean flow gradients around the aerofoil leading edge can produce the distortion of turbulent

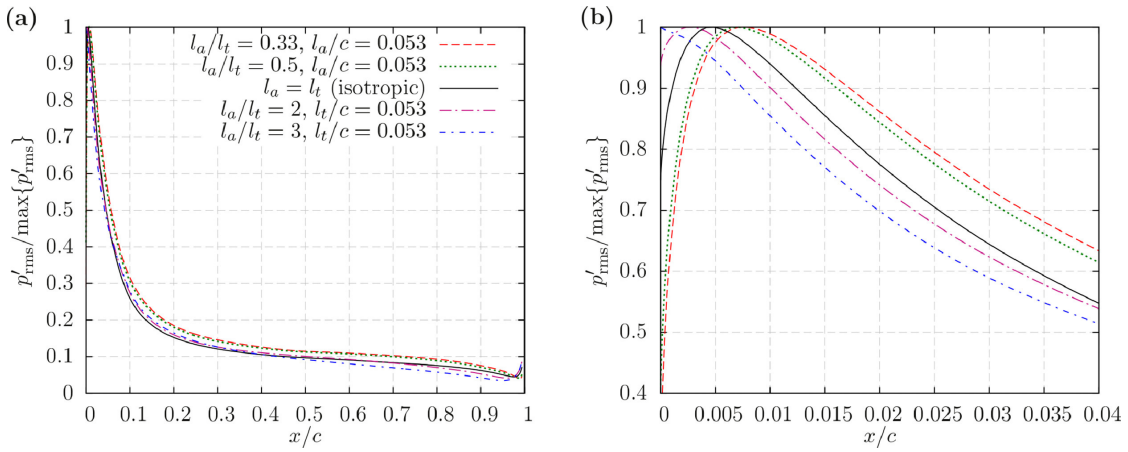

Figure 11: Normalised root-mean-square pressure fluctuations on the surface of a NACA 0012 aerofoil at $M_\infty = 0.3$ and $AoA = 0°$. (a) x/c varying from the leading edge ($x/c = 0$) to the trailing edge ($x/c = 1$). (b) Close-up of the leading edge region, $x/c \leq 0.04$.

structures. This mechanism can partially explain the differences in the aerofoil response and leading edge noise between thick aerofoils and flat plates [3,51]. Fig. 12 shows the distortion of the turbulence spectra along the stagnation line at various locations upstream of the aerofoil leading edge ($x/c = 0$). The distortion of the turbulence spectra are small at $x/c = -0.2$, as $10\log_{10}(E_{ij}/E_{ij,\infty}) \approx 0$ dB. However, significant variations in the spectral content can be found at $x/c = -0.02$. This location corresponds to a distance upstream of the aerofoil that is of the order of the leading edge radius, which can be calculated as $r_{LE}/c = 1.1019(t_A/c)^2$ for a NACA 4-digit aerofoil. In this work, $r_{LE}/c \approx 0.016$ for the NACA 0012 aerofoil. For all cases, the trends are relatively similar. E_{22} presents a significant increase at low frequencies in the vicinity of the aerofoil leading edge, particularly for turbulence stretched in the streamwise direction. However, E_{11} tends to decrease at all frequencies, which is more pronounced for turbulence stretched in the transverse direction. These observations suggest that the transverse turbulence intensity increases and the streamwise turbulence intensity decreases near the stagnation point for all cases. These results are consistent with the findings of Hainaut et al. [51] for isotropic turbulence and Shen and Zhang [52] for anisotropic turbulence with small variations in l_a/l_t.

To study the relationship between the distorted turbulent structures and the unsteady pressure response on the aerofoil surface, the magnitude-squared coherence is defined as

$$\gamma^2_{u_ip}(f) = \frac{|S_{u_ip}(f)|^2}{S_{u_iu_i}(f)\, S_{pp}(f)} \quad , \tag{18}$$

where $S_{u_iu_i}$ is the spectral density of a fluctuating velocity component, u'_i, in the vicinity of the leading edge, and S_{u_ip} is the cross-spectral density between u'_i and p' on the aerofoil surface. Fig. 13 shows the coherence between velocity fluctuations collected at $x/c = -0.02$ along the stagnation line and pressure fluctuations on the surface of a NACA 0012 aerofoil in the leading edge region. The streamwise velocity fluctuations are mainly responsible for the noise radiated from the stagnation point (location A) for all cases, as can be inferred from Fig. 13, in which $\gamma^2_{u_xp} \approx 0.9$ and $\gamma^2_{u_yp} \approx 0.1$ at all frequencies. When moving away from the stagnation point (locations B and C), the transverse velocity fluctuations become increasingly

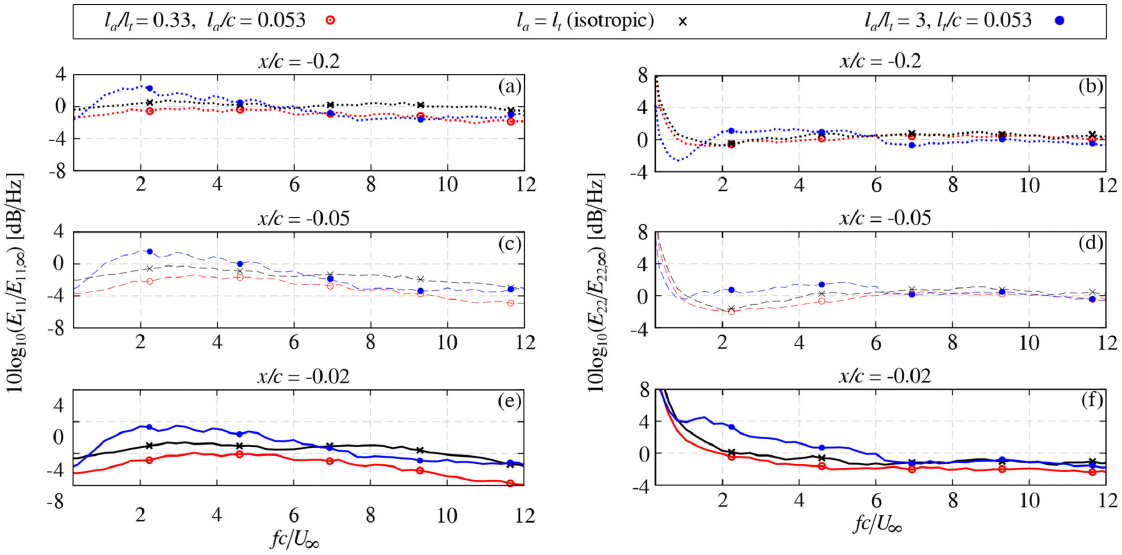

Figure 12: Distortion of one-dimensional spectra along the stagnation line upstream of the leading edge of a NACA 0012 aerofoil in a $M_\infty = 0.3$ flow.

coherent with the unsteady pressure response, particularly at high frequencies. The maximum in p'_{rms}, which occurs at location C approximately for isotropic turbulence, is mainly due to the transverse fluctuating velocity component, which is consistent with the flat plate response.

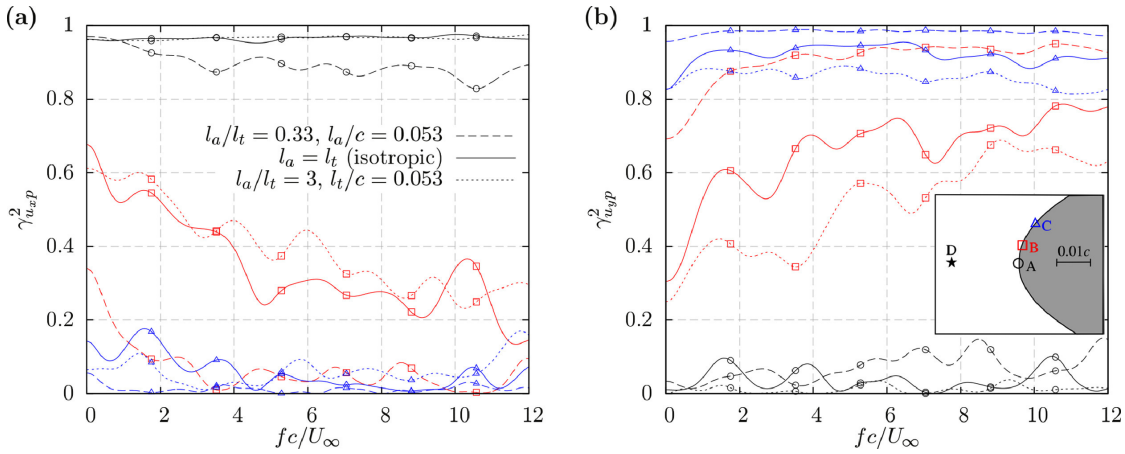

Figure 13: Magnitude-squared coherence between pressure fluctuations at three different locations, A ($x/c = 0$, black lines and circles), B ($x/c \approx 0.001$, red lines and squares) and C ($x/c \approx 0.005$, blue lines and triangles) on the aerofoil surface and velocity fluctuations at location D, which corresponds to $x/c = -0.02$ along the stagnation line. (a) Coherence between pressure fluctuations and streamwise velocity fluctuations. (b) Coherence between pressure fluctuations and transverse velocity fluctuations. (For interpretation of the references to colour in this figure legend, the reader is referred to the web version of this article.)

Fig. 14 (a) shows $\Delta\text{PWL} = \text{PWL}|_{\text{flat plate}} - \text{PWL}|_{\text{NACA0012}}$ as a function of the thickness-based reduced frequency, ft_A/U_∞, which is a useful parameter to quantify the noise reduction. It should be noted that $\text{PWL}|_{\text{flat plate}}$ is computed using the analytical model of Amiet [1], $\text{PWL}|_{\text{NACA0012}}$ is obtained from the CAA methodology for far-field noise predictions presented in Section 4, and t_A corresponds to the maximum aerofoil thickness of the NACA 0012 aerofoil. A significant noise reduction due to aerofoil thickness can be observed in all anisotropic turbulence

cases at high frequencies. Furthermore,ΔPWL spectra follow the same trends as the isotropic turbulence baseline. This implies that the amount of noise reduction due to thickness is nearly independent of the anisotropy in low speed flows.

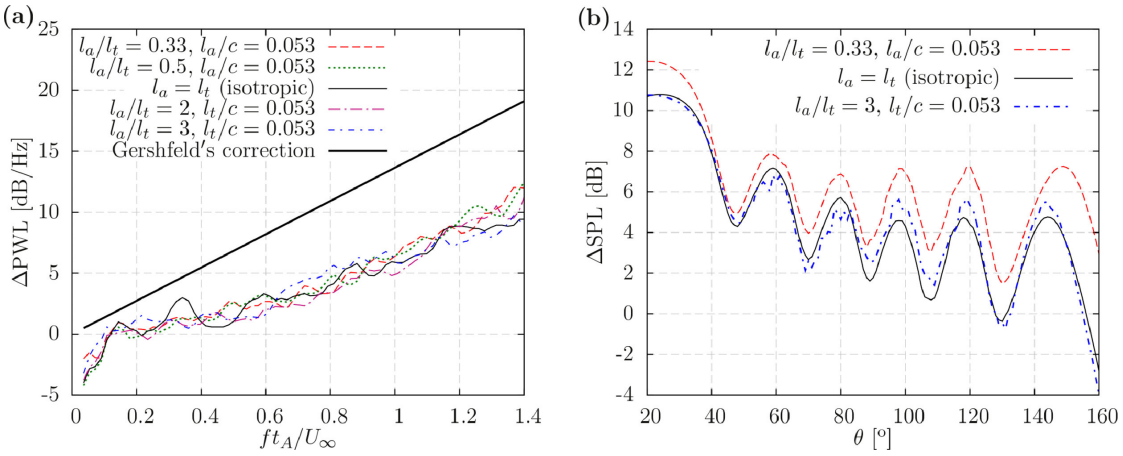

Figure 14: Thickness effect on leading edge noise from a NACA 0012 aerofoil in a $M_\infty = 0.3$ flow at $AoA = 0°$. (a) $\Delta\text{PWL} = \text{PWL}|_{\text{flat plate}} - \text{PWL}|_{\text{NACA0012}}$ spectra with varying l_a/l_t. (b) Directivity of $\Delta\text{SPL} = \text{SPL}|_{\text{flat plate}} - \text{SPL}|_{\text{NACA0012}}$ at $fc/U_\infty = 9$.

The scaling law proposed by Gershfeld [27] to account for aerofoil thickness effects on leading edge noise has also been included in Fig. 14 (a), and takes the form

$$\Delta\text{PWL} = 10\log_{10}\left[\exp\left(\frac{\pi f t_A}{U_\infty}\right)\right] = \log_{10}\left[\exp\left(10\pi\right)\right]\frac{f t_A}{U_\infty} \quad . \tag{19}$$

The scaling law of Gershfeld [27] shows an over-prediction on the noise reduction in comparison with numerical ΔPWL, especially at high frequencies. Similar results were reported by Chaitanya et al. [8] in open-jet wind tunnel experiments of a NACA 0012 aerofoil interacting with nearly isotropic turbulence.

Paterson and Amiet [6] found experimentally a 5 dB noise reduction on a NACA 0012 aerofoil at $ft_A/U_\infty = 1$, which is often used as a reference value for the breakdown of the flat plate assumption. An earlier onset of thickness effects on noise from a NACA 0012 aerofoil has been reported in recent experimental and numerical studies [8,50]. In Fig. 14 (a), a reduction of 5 dB in PWL due to aerofoil thickness is found at approximately $f_t A/U_\infty = 0.9$ for both isotropic and moderately anisotropic turbulence at $M_\infty = 0.3$. This corresponds to a slightly lower frequency than that reported by Paterson and Amiet [6].

Fig. 14 (b) shows the directivity of the noise reduction at $fc/U_\infty = 9$, which corresponds to $ft_A/U_\infty \approx 1.08$. $\Delta\text{SPL} = \text{SPL}|_{\text{flat plate}} - \text{SPL}|_{\text{NACA0012}}$ exhibits a more pronounced noise reduction at downstream observer angles, $\theta < 45°$,for both isotropic and anisotropic turbulence. It can also be observed that anisotropic turbulent flows do not modify the directivity of the leading edge noise from thick aerofoils, as the location of the lobes is similar for l_a/l_t ranging between 0.33 and 3.

5.3 Thick aerofoils in a high-subsonic Mach number flow

The effects of thickness and various mean flow Mach numbers on PWL are shown in Fig. 15 for NACA 0012 aerofoils at $AoA = 0°$. ΔPWL spectra appear to scale linearly with ft_A/U_∞ at $M_\infty = 0.6$ in Fig. 15 (a). The trends are consistent with the results for $M_\infty = 0.3$ in Fig. 14 (a). Nevertheless, the increase in the mean flow Mach number leads to more significant deviations in ΔPWL spectra for the different degrees of anisotropy, as cases with $l_a/l_t > 1$ tend to be about $2-3$ dB louder at all frequencies than cases with $l_a/l_t < 1$. This result is confirmed by examining the variations in OverAll PWL (OAPWL) in Fig. 15 (b). In this work, the OAPWL for each aerofoil configuration is obtained from the integration of the sound power in Eq. (14) for frequencies between $fc/U_\infty = 0.3$ and $fc/U_\infty = 12$, i.e.

$$\text{OAPWL} = 10\log_{10}\left(\frac{\int \mathcal{P}(f)\mathrm{d}f}{\mathcal{P}_{\text{ref}}}\right). \tag{20}$$

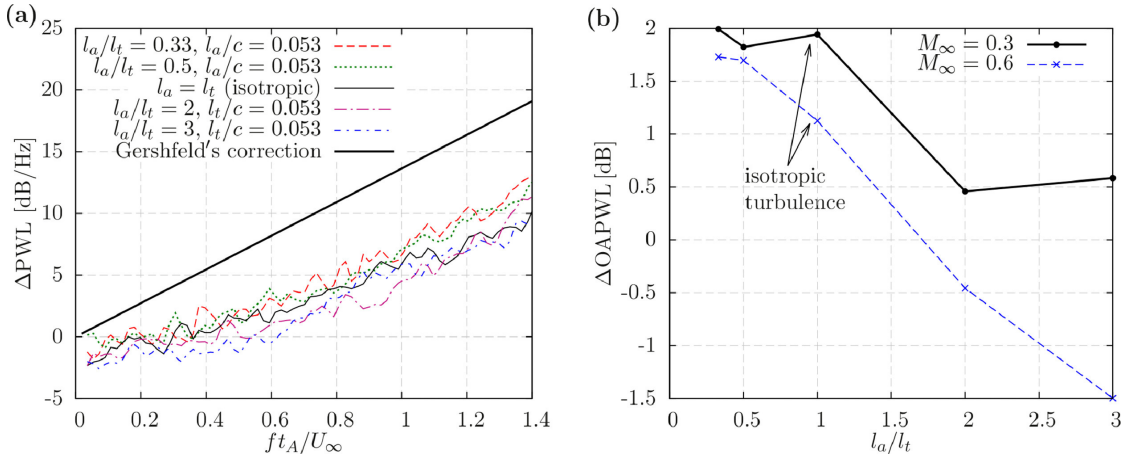

Figure 15: Effects of thickness and mean flow Mach number on leading edge noise from a NACA 0012 aerofoil at $AoA = 0°$. (a) $\Delta\text{PWL} = \text{PWL}|_{\text{flat plate}} - \text{PWL}|_{\text{NACA0012}}$ at $M_\infty = 0.6$. (b) $\Delta\text{OAPWL} = \text{OAPWL}|_{\text{flat plate}} - \text{PWL}|_{\text{NACA0012}}$ for various Mach numbers.

Gill et al. [3] showed that leading edge noise from thick aerofoils at zero angle of attack is mainly generated by the transverse disturbances in isotropic turbulence. This is related to the aerofoil response, which increases for $k_x \to 0$ m^{-1} (low frequencies) and $k_y \to 0$ m^{-1} (gusts that are perpendicular to the aerofoil chord) at $AoA = 0°$ [3,28]. However, the streamwise disturbances become increasingly important in anisotropic turbulence with $l_a/l_t > 1$, which delay the onset of aerofoil thickness effects on leading edge noise and can have a negative impact in terms of ΔOAPWL at high Mach numbers, as shown in Fig. 15 (b). This is likely because as l_a increases, the energy in the wavenumber spectra moves towards lower k_x values (e.g. Fig. 3), for which the aerofoil response is expected to be amplified. Additionally, it can be seen in Fig. 2 that the streamwise turbulence spectrum, E_{11}, presents a larger amplitude than that of the transverse spectrum, E_{22}, for turbulence stretched in the streamwise direction, which reinforces the role of the streamwise disturbances.

In order to better understand the trends in ΔPWL spectra at high Mach number, Fig. 16 shows variations in ΔSPL with frequency and observer angle. Leading edge noise from the NACA 0012 aerofoil can be up to 20 dB louder than the flat plate response in the upstream

direction, which can be attributed to the aerofoil thickness and the streamwise disturbances. This can be observed in some areas where $\Delta\text{SPL} < 0$ dB for $\theta > 90°$, and it is particularly pronounced at low frequencies, $ft_A/U_\infty < 0.6$, and for turbulence stretched in the streamwise direction, $l_a/l_t > 1$. This result is consistent with the work of Zhong and Zhang [31] when studying the influence of the streamwise component on leading edge noise at transonic mean flow speeds. In the downstream direction, $\theta < 90°$, there is a significant noise reduction at most observer angles and frequencies. Larger noise reductions are found for turbulence stretched in the transverse direction, $l_a/l_t < 1$, especially at high frequencies.

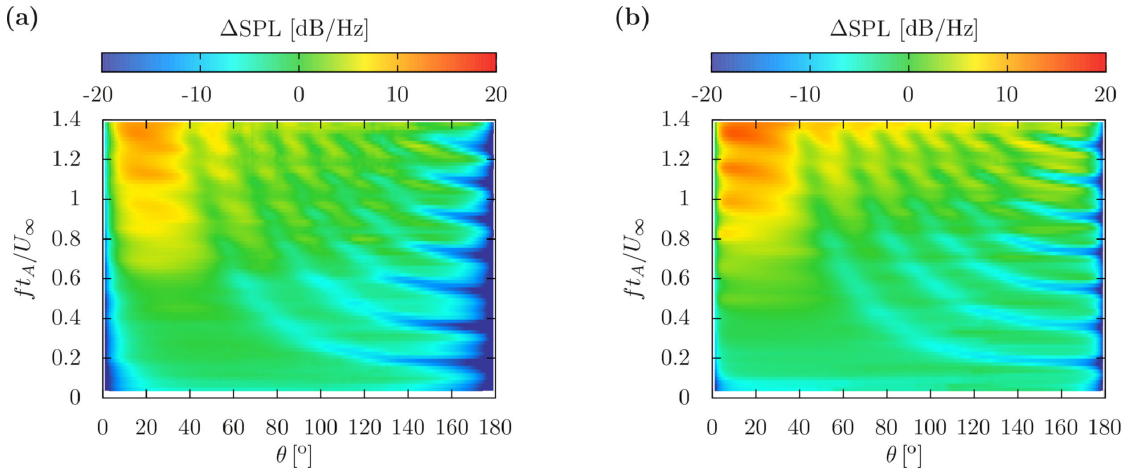

Figure 16: Contours of $\Delta\text{SPL} = \text{SPL}|_{\text{flat plate}} - \text{SPL}|_{\text{NACA0012}}$ in a $M_\infty = 0.6$ flow at $AoA = 0°$. (a) $l_a/l_t = 3$. (b) $l_a/l_t = 0.33$.

5.4 Thick aerofoils at non-zero angle of attack

In this section, the NACA 0012 aerofoil is rotated around its leading edge at $AoA = 6°$, as shown in Figs. 4 and 5. An inviscid mean flow with freestream Mach number $M_\infty = 0.3$ is used in CAA simulations. This aerofoil configuration presents an attached subsonic flow around the aerofoil, and therefore it is convenient to study possible effects of angle of attack on leading edge noise.

Fig. 17 shows normalised p'_{rms} along the aerofoil chord. The aerofoil response shows a similar distribution on the suction side for different degrees of anisotropy. It can also be seen that noise is mainly generated on the suction side near the leading edge, where the maximum in p'_{rms} occurs for all the cases. However, some differences can be found on the pressure side. The asymmetry in the p'_{rms} distribution on both sides of the aerofoil is due to angle of attack, and becomes more pronounced with low values of l_a/l_t. For example, cases with turbulence stretched in the transverse direction show low $p'_{\text{rms}}/\max\{p'_{\text{rms}}\}$ values and a new peak appears to develop between $x/c = 0.01$ and $x/c = 0.02$. This suggests that noise generated from the pressure side becomes increasingly important for aerofoils at $AoA \neq 0°$ when $l_a/l_t < 1$.

Fig. 18 (a) shows PWL spectra of a NACA 0012 aerofoil at non-zero angle of attack compared against simulations at $AoA = 0°$ from Section 5.2. PWL spectra show that an increase in angle of attack reduces the leading edge noise of a thick aerofoil in anisotropic turbulence with $l_a/l_t < 1$, especially at high frequencies. It is well known that synthetic turbulence that

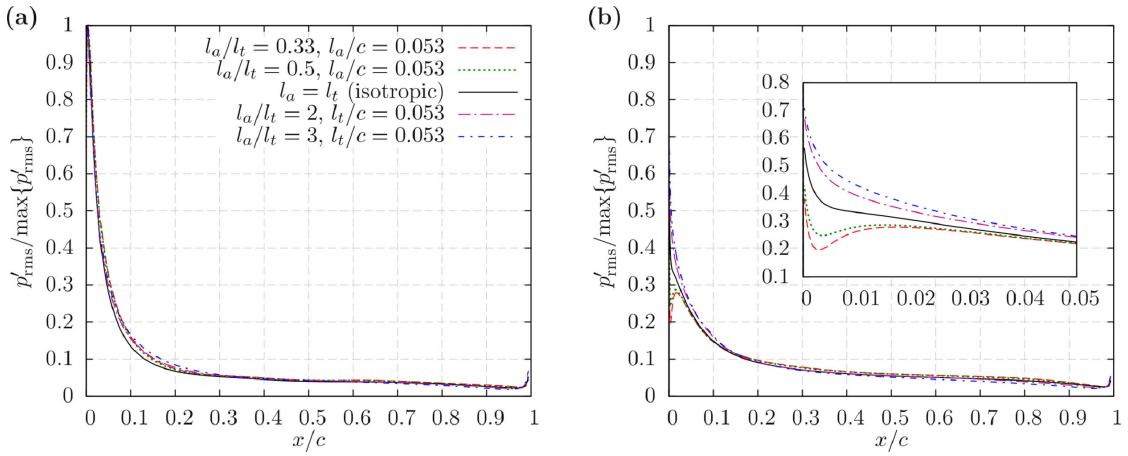

Figure 17: Normalised root-mean-square pressure fluctuations on the surface of a NACA 0012 aerofoil at $M_\infty = 0.3$ and $AoA = 6°$. (a) Suction side. (b) Pressure side.

only enforces the transverse velocity disturbances ($k_y = 0$ m^{-1}) under-predicts the leading edge noise from thick aerofoils at non- zero angle of attack [3,5]. This phenomenon may also occur in anisotropic turbulence with $l_a/l_t < 1$, since the transverse velocity disturbances become notably larger than the streamwise disturbances and are thus the dominant disturbances. The physical mechanism behind this behaviour is related to a shift in the energy of the velocity spectra, which moves towards low k_y values as l_t increases (e.g. Fig. 3). However, the maximum in the aerofoil response follows opposite trends, and shifts towards $k_y > 0$ m^{-1} as the angle of attack increases [3,28], particularly at high frequencies.

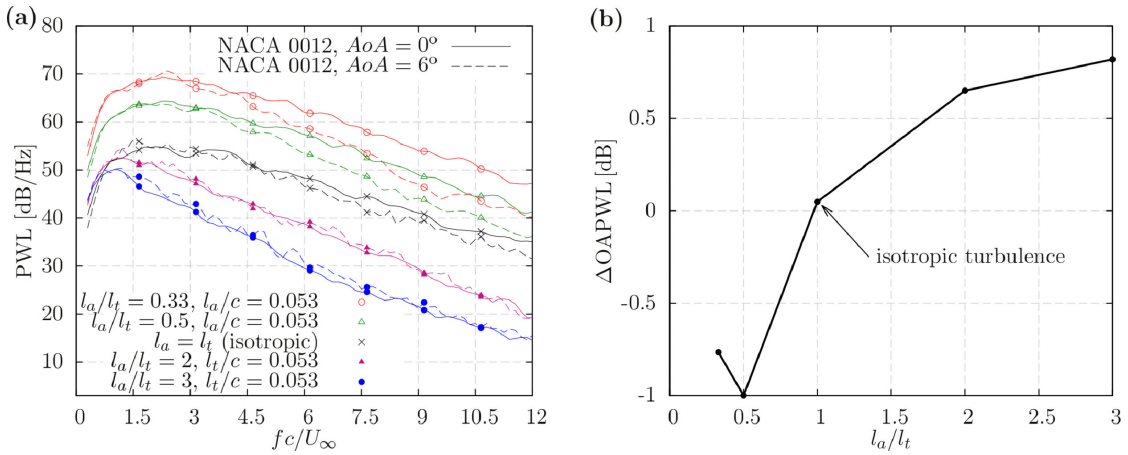

Figure 18: Noise spectra from anisotropic turbulence interacting with a NACA 0012 aerofoil at $M_\infty = 0.3$ and $AoA = 6°$. (a) PWL spectra. (b) ΔOAPWL = OAPWL$|_{AoA=6°}$ − OAPWL$|_{AoA=0°}$.

In anisotropic turbulence with $l_a/l_t > 1$, PWL spectra present an increase of about 1 dB at all frequencies. Such an increase is within the level of accuracy of the current simulations, however the result indicates that a moderate increase in the angle of attack has a reduced impact on the PWL spectra from thick aerofoils. This contrasts with the work of Devenport et al. [28], who showed an increase in 1/3rd octave band SPL of approximately 5 dB for every 4° increment at low frequencies for a NACA 0015 aerofoil in a $M_\infty = 0.08$ flow with $l_a/l_t = 2$, suggesting

a stronger effect of anisotropy on noise. The noise predictions of the current work have been successfully validated by using an analytical flat plate model [1] in Section 5.1 and agree with the trends reported in experimental measurements. For example, Paterson and Amiet [6] found that the effect of angle of attack on leading edge noise was negligible for a NACA 0012 aerofoil, despite correcting the von Kármán isotropic spectrum with a contracted spanwise correlation length to account for some anisotropy in the flow.

The discrepancy with the conclusions made by Devenport et al. [28] can be due to the different assumptions involved in the numerical methodologies. Devenport et al. [28] used a panel method that is valid for leading edge noise predictions of aerofoils in incompressible flows, i.e. low Mach numbers, whereas the LEEs can simulate compressible subsonic flows. Furthermore, the panel method assumed the aerofoil to be acoustically compact, which implies that the acoustic wavelength is significantly larger than the aerofoil chord. Consequently, the noise predictions of Devenport et al. [28] are only valid for frequencies below 1000 Hz. The validity of the results presented in the current work extends to frequencies up to $fc/U_\infty = 12$ in a $M_\infty = 0.3$ flow, which corresponds to 8160 Hz. Furthermore, the loss of compactness, which causes directivity lobes at high frequencies, is correctly modelled by the LEEs (e.g. Fig. 9).

Variations in $\Delta\text{OAPWL} = \text{OAPWL}|_{AoA=6^\circ} - \text{OAPWL}|_{AoA=0^\circ}$ for different l_a/l_t are shown in Fig. 18 (b). The ΔOAPWL calculation indicates that a moderate variation in angle of attack has a small effect on aerofoils interacting with isotropic turbulence, as $\Delta\text{OAPWL} \approx 0$ dB. However, there is an increase (< 1 dB) in the noise when turbulence is stretched in the streamwise direction, $l_a/l_t > 1$, and a decrease as turbulence is stretched in the transverse direction, $l_a/l_t < 1$. It should be noted that the OAPWL is mainly dominated by low frequencies with large sound levels. This can mask differences in the PWL spectra at high frequencies. Overall, the effect of the angle of attack on leading edge noise due to moderately anisotropic turbulence is small, with differences in ΔOAPWL smaller than 1 dB for l_a/l_t ranging from 0.33 to 3.

Fig. 19 shows directivity plots of NACA 0012 aerofoils at various chord-based Strouhal numbers and l_a/l_t. The leading edge noise reduction that was identified for the aerofoil at $AoA = 6^\circ$ in anisotropic turbulence with $l_a/l_t < 1$ is mainly produced at downstream observer angles above the aerofoil, $\theta < 90^\circ$. Additionally, it can be observed that variations in angle of attack have a limited impact for observers below the aerofoil, which may be attributed to the peak in p'_{rms} that appears on the pressure side when $l_a/l_t < 1$, as shown in Fig. 17 (b). For cases with anisotropic turbulence stretched in the streamwise direction, small variations in SPL are found for mid-range and high frequencies, and similar noise levels can be observed above and below the aerofoil at both $AoA = 0^\circ$ and $AoA = 6^\circ$.

5.5 Effect of turbulence length scales

In this work, leading edge noise predictions have been performed for aerofoils with small values of turbulence length scale-to-chord ratio, as occurs in turbofan engines (see Table 2). Using this assumption, this section presents simulations of a NACA 0012 aerofoil in a $M_\infty = 0.3$ flow at $AoA = 0^\circ$ and $AoA = 6^\circ$ with twice the baseline turbulence length scale (0.016 m instead of 0.008 m). The objective is to assess whether variations in l_a/c and l_t/t_A can affect the

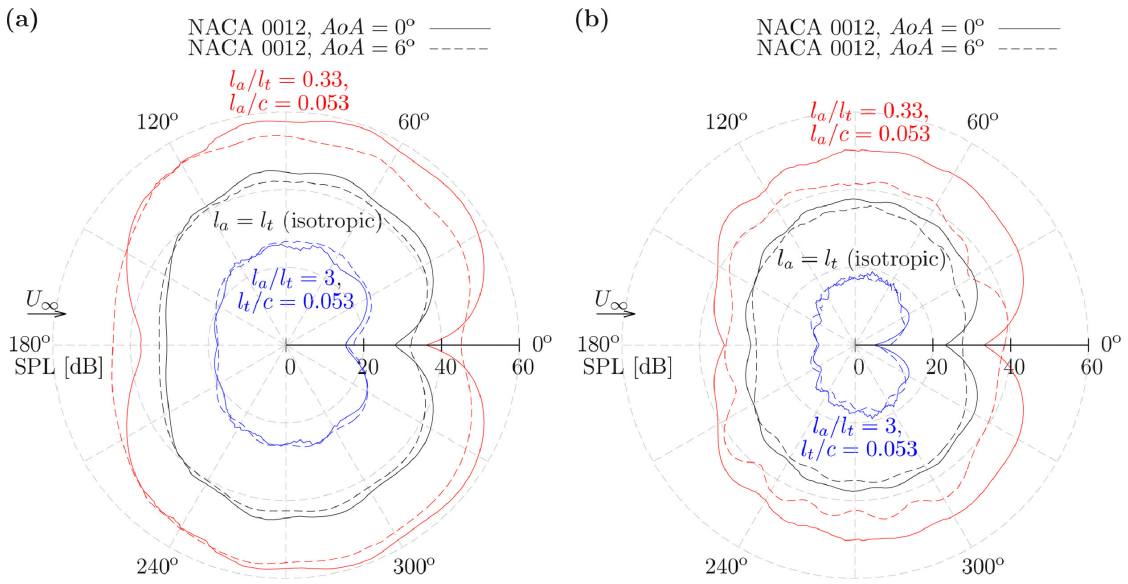

Figure 19: Directivity plots for a NACA 0012 aerofoil at $AoA = 0°$ and $AoA = 6°$ in a $M_\infty = 0.3$ flow. (a) $fc/U_\infty = 6$. (b) $fc/U_\infty = 9$.

conclusions drawn in the previous sections. The configurations studied are given in Table 3.

Table 3: Comparison of turbulence length scales for the various anisotropic turbulence cases (Section 5.5).

l_a [m]	l_t [m]	l_a/l_t	l_a/c	l_t/c	l_t/t_A (NACA 0012)
0.032	0.016	2	0.213	0.107	0.889
0.016	0.032	0.5	0.107	0.213	1.778

Fig. 20 shows the PWL spectra for the CAA simulations with increased length scales. For cases with $l_a/l_t = 2$, a 10 dB noise reduction is found at $fc/U_\infty = 12$ for the NACA 0012 aerofoils at $AoA = 0°$ and 6° compared to the flat plate prediction, which is relatively similar to the noise reduction shown in Fig. 18 (a). In this case, the effect of angle of attack on leading edge noise is small. In contrast, a significant noise reduction is found for the angle of attack configuration with $l_a/l_t = 0.5$. These results suggest that variations in the turbulence length scales do not significantly alter the conclusions of Sections 5.2 and 5.4 for the effects of anisotropy on leading edge noise, if l_a/l_t is kept constant and turbulence length scales are small in comparison with the aerofoil chord.

6 Conclusions

This paper presents a number of CAA simulations to assess the effects of anisotropic turbulence on leading edge noise, which is a dominant source of broadband noise in aero-engines. The numerical methodology combines a synthetic turbulence method with a CAA code that solves the LEEs. An anisotropic synthetic turbulence method is presented to reproduce homogeneous axisymmetric turbulence with $k_z = 0$ m^{-1} for varying streamwise-to-transverse ratios, l_a/l_t, between 0.33 and 3. The aerofoil response is computed from two-dimensional CAA

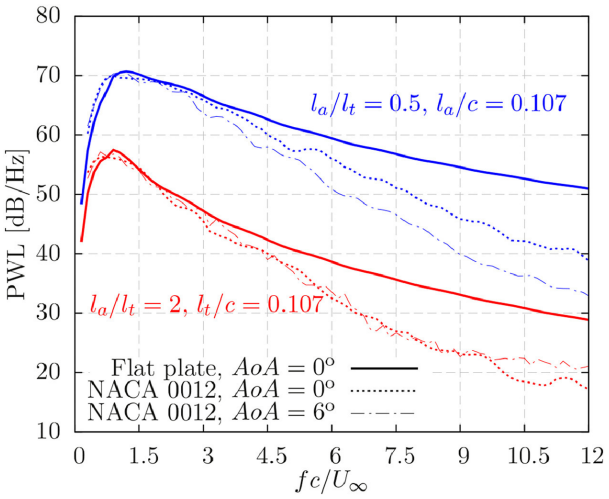

Figure 20: PWL spectra of NACA 0012 aerofoils (from CAA simulations) and flat plates (from Amiet's theory [1]) for increased values of l_a/c and l_t/c.

simulations using inviscid mean flows. Then, far-field noise predictions are obtained from a three-dimensional FW-H solver without including spanwise correlation effects. This numerical methodology has successfully been validated using an analytical flat plate model and NACA 0001 aerofoils.

Anisotropic turbulence produces a redistribution of the energy in the velocity spectra, which has a direct impact on the sound power spectra. This redistribution modifies the amount of energy in the turbulent flow that can contribute to the leading edge noise. It has been shown that increasing the axial length scale shifts the frequency at which the noise spectrum is at a maximum. However, the transverse length scale acts as a scaling factor to the noise spectra, and does not modify the frequency at which the maximum noise level occurs. These results can explain the trends and observations made from cascade models when using anisotropic turbulence. For thin aerofoils, $t_A/c < 0.01$, the transverse velocity spectrum is the main contributor to the leading edge noise for the various l_a/l_t tested. Sound directivity remains unchanged by anisotropy in the flow, as the location of the directivity lobes occurs at the same observer angles for the frequencies examined.

A comprehensive parameter study has been performed to assess the effects of anisotropic turbulence on leading edge noise, including variations in aerofoil thickness, mean flow Mach number, and angle of attack. Noise reduction due to aerofoil thickness at high frequencies occurs for all l_a/l_t tested. Particularly, $\Delta\text{PWL} = \text{PWL}|_{\text{flat plate}} - \text{PWL}|_{\text{NACA0012}}$ spectra vary as a linear function of f/U_∞. The scaling law of Gershfeld [27] has been found to over-estimate the noise reduction, especially at high frequencies. Overall, there is a good overlap with anisotropy in the amount of noise reduction at low speed, $M_\infty = 0.3$, from numerical simulations of NACA 0012 aerofoils at $AoA = 0°$. This suggests that the effects of moderately anisotropic turbulence on the noise reduction due to aerofoil thickness are small at low Mach numbers. Nevertheless, the contribution of the streamwise velocity disturbances appears to become increasingly important for thick aerofoils. For example, the maximum in p'_{rms} moves towards the stagnation point as l_a/l_t increases. This is due to the streamwise velocity fluctuations, as found from the analysis of the magnitude-squared coherence between pressure fluctuations and distorted turbulent

structures in the leading edge region.

As the mean flow Mach number is increased ($M_\infty = 0.6$), the onset of noise reduction due to aerofoil thickness presents a certain l_a/l_t dependency, which has an impact on the overall sound power level. For example, $\Delta\text{OAPWL} = \text{OAPWL}|_{\text{flat plate}} - \text{OAPWL}|_{\text{NACA0012}}$ varies from 2 dB to 1.5 dB as l_a/l_t varies between 0.33 and 3, respectively. A significant noise increase from thick aerofoils has been found at upstream observer locations, which is particularly pronounced for turbulence stretched in the streamwise direction, $l_a/l_t > 1$, at low frequencies, $ft_A/U_\infty < 0.6$. This is related to the streamwise disturbances and their spectral content, which present a larger amplitude than that of the transverse spectrum when $l_a/l_t > 1$ for most frequencies.

An angle of attack increase of 6° shows a small increase of approximately 1 dB on PWL spectra of a NACA 0012 aerofoil in anisotropic turbulence with $l_a/l_t > 1$. In contrast, PWL spectra present a strong decay rate at high frequencies when $l_a/l_t < 1$, which is due to the noise reduction at downstream observer angles above the aerofoil. This phenomenon is attributed to the shift in the energy of the velocity spectra towards $k_y \to 0$ m^{-1}, for which the aerofoil response is expected to be reduced when $AoA \neq 0°$.

Future applications of the current CAA methodology could focus on modelling the anisotropy in the fan wakes with a synthetic turbulence method, and the interaction of anisotropic turbulence with aerofoil cascades. Fully three-dimensional aerofoils, such as swept or wavy leading edge aerofoils, interacting with anisotropic turbulence may also be relevant for aerospace applications.

Acknowledgments

The research funding for this project was partially provided by the University of Southampton and Innovate UK (GA no. 101367), within the framework of the wHole AiRcraft Multidisciplinary nOise desigN sYstem (HARMONY) programme. The IRIDIS 4 High Performance Computing Facility and IT services at the University of Southampton are also acknowledged in the completion of this work.

Appendix A. Input parameters for anisotropic Gaussian superposition

In this appendix, representative values of $u'_{0,n}, l_{x,n}$ and $l_{y,n}$ are given for the anisotropic Gaussian superposition presented in Section 3. These values were found by fitting N_e anisotropic Gaussian velocity spectra from Eqs. (1) – (3) with the homogeneous axisymmetric spectra in Eqs. (9) and (10). It should be noted that there is not a unique set of values for $u'_{0,n}, l_{x,n}$ and $l_{y,n}$ that can be used to reproduce a target anisotropic turbulence spectrum. Nevertheless, the values presented in this appendix provide an accuracy better than 1.5 dB for frequencies up to $fc/U_\infty \leq 12$.

Table A.1 presents the parameters for $N_e = 4$ anisotropic Gaussian spectra to reproduce the isotropic Liepmann spectrum with $u'_a = 0.017U_\infty$ and $l_a = l_t = 0.008$ m. This case corresponds to the baseline configuration for the study of the effects of anisotropic turbulence on leading edge noise. Tables A.2 and A.3 present parameters to generate anisotropic turbulence with

$l_a/l_t > 1$ using $N_e = 5$ anisotropic Gaussian spectra. It can be observed that only one length scale is varied at a time from the baseline configuration for each case of study. Tables A.4 and A.5 present parameters to generate anisotropic turbulence with $l_a/l_t < 1$.

Table A.1: Parameters for Gaussian superposition to generate a two-dimensional fluctuating velocity field with the statistics of isotropic turbulence [18] assuming $k_z = 0\,\mathrm{m}^{-1}$ with $u'_a/U_\infty = 0.017$ and $l_a = l_t = 0.008\,\mathrm{m}$

nth Gaussian eddy	$l_{x,n} = l_{y,n}$ [m]	$u^2_{0,n}$ [m^2/s^2] ($M_\infty = 0.3$)	$u^2_{0,n}$ [m^2/s^2] ($M_\infty = 0.6$)
1	2.35×10^{-2}	7.38×10^{-4}	3.0×10^{-3}
2	1.3×10^{-2}	1.77×10^{-3}	7.0×10^{-3}
3	7.2×10^{-3}	7.1×10^{-4}	2.5×10^{-3}
4	5.0×10^{-3}	5.0×10^{-4}	2.0×10^{-3}

Table A.2: Parameters for Gaussian superposition to generate a two-dimensional fluctuating velocity field with the statistics of axisymmetric turbulence [18] assuming $k_z = 0\,\mathrm{m}^{-1}$ with $u'_a/U_\infty = 0.017$, $l_a/l_t = 2$ and $l_t = 0.008\,\mathrm{m}$

nth Gaussian eddy	$l_{x,n}$ [m]	$l_{y,n}$ [m]	$u^2_{0,n}$ [m^2/s^2] ($M_\infty = 0.3$)	$u^2_{0,n}$ [m^2/s^2] ($M_\infty = 0.6$)
1	4.7×10^{-2}	2.35×10^{-2}	3.9×10^{-4}	1.56×10^{-3}
2	2.6×10^{-2}	1.3×10^{-2}	9.0×10^{-4}	3.6×10^{-3}
3	1.42×10^{-2}	7.2×10^{-3}	4.2×10^{-4}	1.68×10^{-3}
4	8.0×10^{-3}	4.0×10^{-3}	7.2×10^{-4}	7.2×10^{-4}
5	4.4×10^{-3}	8.0×10^{-3}	4.5×10^{-6}	1.8×10^{-5}

Table A.3: Parameters for Gaussian superposition to generate a two-dimensional fluctuating velocity field with the statistics of axisymmetric turbulence [18] assuming $k_z = 0\,\mathrm{m}^{-1}$ with $u'_a/U_\infty = 0.017$, $l_a/l_t = 3$ and $l_t = 0.008\,\mathrm{m}$

nth Gaussian eddy	$l_{x,n}$ [m]	$l_{y,n}$ [m]	$u^2_{0,n}$ [m^2/s^2] ($M_\infty = 0.3$)	$u^2_{0,n}$ [m^2/s^2] ($M_\infty = 0.6$)
1	7.5×10^{-2}	2.5×10^{-2}	1.4×10^{-4}	6.5×10^{-4}
2	4.7×10^{-2}	1.65×10^{-2}	4.6×10^{-4}	1.91×10^{-3}
3	2.8×10^{-2}	9.5×10^{-3}	4.1×10^{-4}	1.45×10^{-3}
4	1.5×10^{-2}	5.1×10^{-3}	2.2×10^{-4}	8.5×10^{-4}
5	6.55×10^{-3}	4.0×10^{-3}	1.6×10^{-5}	6.4×10^{-5}

Appendix B. Analytical flat plate model for leading edge noise prediction

This appendix presents the main equations of the analytical flat plate model that has been used in this work. For further details, the reader is referred to the work of Amiet [1,6].

The power spectral density of far-field sound can be written as,

$$S_{pp}(r_0, \theta, \omega) = \frac{\pi \rho_0^2 b^2 d \sin^2\theta U_\infty \kappa_0^2}{2 r_0^2 A(\theta, M_\infty)^4} \, \Phi_{22}(k_x, k_z = 0) \, |\mathcal{L}(\theta, k_x)|^2 \quad , \tag{B.1}$$

Table A.4: Parameters for Gaussian superposition to generate a two-dimensional fluctuating velocity field with the statistics of axisymmetric turbulence [18] assuming $k_z = 0\,\mathrm{m}^{-1}$ with $u'_a/U_\infty = 0.017$, $l_a/l_t = 0.5$ and $l_a = 0.008\,\mathrm{m}$

nth Gaussian eddy	$l_{x,n}$ [m]	$l_{y,n}$ [m]	$u^2_{0,n}$ [m^2/s^2] ($M_\infty = 0.3$)	$u^2_{0,n}$ [m^2/s^2] ($M_\infty = 0.6$)
1	2.1×10^{-2}	4.1×10^{-2}	4.7×10^{-3}	1.9×10^{-2}
2	1.05×10^{-2}	2.1×10^{-2}	7.8×10^{-3}	3.0×10^{-2}
3	4.7×10^{-3}	9.6×10^{-3}	2.5×10^{-4}	1.0×10^{-4}
4	5.3×10^{-3}	4.9×10^{-3}	1.8×10^{-4}	7.0×10^{-4}
5	5.0×10^{-3}	1.3×10^{-2}	1.0×10^{-5}	4.0×10^{-5}

Table A.5: Parameters for Gaussian superposition to generate a two-dimensional fluctuating velocity field with the statistics of axisymmetric turbulence [18] assuming $k_z = 0\,\mathrm{m}^{-1}$ with $u'_a/U_\infty = 0.017$, $l_a/l_t = 0.33$ and $l_a = 0.008\,\mathrm{m}$

nth Gaussian eddy	$l_{x,n}$ [m]	$l_{y,n}$ [m]	$u^2_{0,n}$ [m^2/s^2] ($M_\infty = 0.3$)	$u^2_{0,n}$ [m^2/s^2] ($M_\infty = 0.6$)
1	2.5×10^{-2}	7.8×10^{-2}	4.0×10^{-3}	1.6×10^{-2}
2	1.65×10^{-2}	4.7×10^{-2}	1.15×10^{-2}	4.6×10^{-2}
3	9.5×10^{-3}	2.8×10^{-2}	1.2×10^{-2}	4.8×10^{-2}
4	5.1×10^{-3}	1.5×10^{-2}	6.0×10^{-3}	2.4×10^{-2}
5	4.0×10^{-3}	6.55×10^{-3}	4.8×10^{-4}	1.9×10^{-3}

where $\kappa_0 = \omega/c_\infty$, is the acoustic wavenumber, $\omega = 2\pi f$ is the angular frequency, $b = c/2$ is the aerofoil semi-chord.

The non-dimensional unsteady loading term, $\mathcal{L}(\theta, k_x)$, is given at low acoustic reduced frequencies, $\mu_a = k_x M_\infty b/\beta^2 < \pi/4$, by [53]

$$\mathcal{L}_{\mathrm{low}}(\theta, k_x) = \frac{1}{\beta} S(\mu_h) \exp[\mathrm{i}\mu_h f(M_\infty)] \left\{ J_0\left(\frac{\mu_a M_\infty \cos\theta}{A(\theta, M_\infty)}\right) - \mathrm{i} J_1\left(\frac{\mu_a M_\infty \cos\theta}{A(\theta, M_\infty)}\right) \right\} \ , \tag{B.2}$$

where J_0 and J_1 are Bessel functions of the first kind, $\mu_h = k_x b/\beta^2$ is the hydrodynamic reduced frequency, $f(M_\infty) = (1-\beta)\ln(M_\infty) + \beta\ln(1+\beta) - \ln(2)$ is a phase correction factor, and $S(\mu_h)$ represents the Sears function, which is defined by means of the Hankel functions of the second kind ($H_0^{(2)}$ and $H_1^{(2)}$),

$$S(\mu_h) = \frac{2}{\pi\mu_h \left[H_0^{(2)}(\mu_h) - \mathrm{i}H_1^{(2)}(\mu_h)\right]} \ . \tag{B.3}$$

At high acoustic reduced frequencies, $\mu_a > \pi/4$, the non-dimensional unsteady loading term $\mathcal{L}(\theta, k_x)$ is split into two contributions [54].

$$\mathcal{L}_{\mathrm{high}}(\theta, k_x) = \mathcal{L}_1(\theta, k_x) + \mathcal{L}_2(\theta, k_x) \ , \tag{B.4}$$

where $\mathcal{L}_1(\theta, k_x)$ corresponds to the main leading edge scattering half-plane problem,

$$\mathcal{L}_1(\theta, k_x) = \frac{\sqrt{2}E_f^*(2\Theta_1)\exp(\mathrm{i}\Theta_2)}{\pi\beta\sqrt{\mu_h(1+M_\infty)\,\Theta_1}}, \tag{B.5}$$

which is corrected by the solution of the back scattering trailing edge problem,

$$\mathcal{L}_2(\theta, k_x) = \frac{\exp(\mathrm{i}\Theta_2)\left\{\mathrm{i}\big(1-\exp(-\mathrm{i}2\Theta_1)\big) + (1-\mathrm{i})\left[E_f^*(4\mu_a) - \sqrt{\frac{2}{1+\cos\theta/A(\theta,M_\infty)}}E_f^*(2\Theta_3)\exp(-\mathrm{i}2\Theta_1)\right]\right\}}{\pi\Theta_1\beta\sqrt{2\pi\mu_h(1+M_\infty)}}. \tag{B.6}$$

In Eqs. (B.5) and (B.6), the following terms have been introduced to simplify the notation

$$\begin{aligned}
\Theta_1 &= \mu_a\Big(1 - \frac{\cos\theta}{A(\theta, M_\infty)}\Big),\\
\Theta_2 &= \mu_a\Big(M_\infty - \frac{\cos\theta}{A(\theta, M_\infty)}\Big) - \frac{\pi}{4},\\
\Theta_3 &= \mu_a\Big(1 + \frac{\cos\theta}{A(\theta, M_\infty)}\Big),
\end{aligned} \tag{B.7}$$

and E_f^* represents the conjugate of the Fresnel integral, which is defined as

$$E_f^*(\Theta) = \frac{1}{\sqrt{2\pi}}\int_0^\Theta \frac{\exp(-i\xi)}{\sqrt{\xi}}\,\mathrm{d}\xi. \tag{B.8}$$

References

1. R.K. Amiet, Acoustic radiation from an airfoil in a turbulent stream, J. Sound Vib. 41 (1975) 407–420. doi:10.1016/0022-460X(75)90102-5.

2. V.P. Blandeau, P.F. Joseph, G. Jenkins, C.J. Powles, Comparison of sound power radiation from isolated airfoils and cascades in a turbulent flow, J. Acoust. Soc. Am. 129 (2011) 3521–3535. doi:10.1121/1.35695706.

3. J. Gill, X. Zhang, P. Joseph, Single velocity broadband-component modeling of leading edge turbulence interaction noise, J. Acoust. Soc. Am. 137 (2015) 3209–3220. doi:10.1121/1.4921492.

4. D. Kim, G.-S. Lee, C. Cheong, Inflow noise from an isolated symmetric airfoil interacting with incident turbulence, J. Fluids Struct. 55 (2015) 428–450. doi:10.1016/j.jfluidstructs.2015.03.015.

5. F. Gea-Aguilera, J. Gill, X. Zhang, Synthetic methods for computational simulations of leading edge noise, Comput. Fluids 157 (2017) 240–252. doi:10.1016/j.compfluid.2017.08.039.

6. R.W. Paterson, R.K. Amiet, Acoustic radiation and surface pressure characteristics of an airfoil due to incident turbulence, NASA Tech. Rep., CR-2733, 1976.

7. S. Moreau, M. Roger, V. Jurdic, Effect of angle of attack and airfoil shape on turbulence-interaction noise, 11th AIAA/CEAS Aeroacoustics Conference, Monterey, CA, 2005.

8. P. Chaitanya, J. Gill, S. Narayanan, P. Joseph, C. Vanderwel, X. Zhang, B. Ganapathisubramani, Aerofoil geometry effects on turbulence-interaction noise, 21st AIAA/CEAS Aeroacoustics Conference, Dallas, TX, 2015. doi:10.2514/6.2015-2830.

9. D.B. Hanson, Spectrum of rotor noise caused by atmospheric turbulence, J. Acoust. Soc. Am. 56 (1974) 110–126, doi: 10.1121/1.1903241.

10. R.A. Kantola, R.E. Warren, Flight noise simulation in an anechoic chamber, AIAA J. 19 (1981) 350–357, doi: 10.2514/3.50955.

11. G.G. Podboy, M.J. Krupar, S.M. Helland, C.E. Hughes, Steady and unsteady flow field measurements within a NASA 22 inch fan model, 40th AIAA Aerospace Sciences Meeting and Exhibit, Reno, NV, 2002. doi:10.2514/6.2002-1033.

12. G. Jenkin, Models for the prediction of rear-arc and forward-arc fan broadband noise in turbofan engines, Ph.D. Thesis, Cranfield University, 2011.

13. R. Karve, D. Angland, T. Node-Langlois, An analytical model for predicting rotor broadband noise due to turbulent boundary layer ingestion, J. Sound Vib. 436 (2018) 62–80. doi:10.1016/j.jsv.2018.08.020.

14. R.W. Paterson, R.K. Amiet, Noise of a model helicopter rotor due to ingestion of turbulence, 1979, NASA Tech. Rep., CR-3213.

15. R.J. Astley, A. Agarwal, K.R. Holland, P.F. Joseph, M.G. Smith, R. Sugimoto, B.J. Tester, Predicting and reducing aircraft airframe noise, 14th International Congress on Sound and Vibration, Cairns, Australia, 2007.

16. U.W. Ganz, P.D. Joppa, T.J. Patten, D.F. Scharpf, Boeing 18-inch fan rig broadband noise test, NASA Tech. Rep., CR-1998-208704, 1998.

17. S.B. Pope, Turbulent Flows, Cambridge University Press, 2000.

18. E.J. Kerschen, P.R. Gliebe, Noise caused by the interaction of a rotor with anisotropic turbulence, AIAA J. 19 (1981) 717–723. doi:10.2514/3.50995.

19. S. Glegg, N. Walker, Fan noise from blades moving through boundary layer turbulence, in: 5th AIAA/CEAS Aeroacoustics Conference, Bellevue, Wash- ington, 1999, doi: 10.2514/6.1999-1888.

20. S. Chandrasekhar, The theory of axisymmetric turbulence, Philos. Trans. R. Soc. Lond. Ser. A 242 (1950) 557–577. doi:10.1098/rsta.1950.0010.

21. H.M. Atassi, M.M. Logue, Fan broadband noise in anisotropic turbulence, 15th AIAA/CEAS Aeroacoustics Conference, Miami, FL, 2009. doi:10.2514/6.2009-3148.

22. G.K. Batchelor, I. Proudman, The effect of rapid distortion of a fluid in turbulent motion, Q. J. Mech. Appl. Math. 7 (1954) 83–103. doi:10.1093/qjmam/7.1.83.

23. D.B. Hanson, Theory for broadband noise of rotor and stator cascades with inhomogeneous inflow turbulence including effects of lean and sweep, NASA Tech. Rep., CP-2001-210762, 2001.

24. H. Posson, S. Moreau, M. Roger, Broadband noise prediction of fan outlet guide vane using a cascade response function, J. Sound Vib. 330 (2011) 6153–6183. doi:10.1016/j.jsv.2011.07.040.

25. W. Olsen, J. Wagner, Effect of thickness on airfoil surface noise, AIAA J. 20 (1982) 437–439. doi:10.2514/3.7922.

26. A.M. Hall, O.V. Atassi, J. Gilson, R. Reba, D. Shannon, Effect of leading-edge thickness on high-speed airfoil-turbulence interaction noise, 17th AIAA/CEAS Aeroacoustics Conference, Portland, OR, 2011. doi:10.2514/6.2011-2861.

27. J. Gershfeld, Leading edge noise from thick foils in turbulent flows, J. Acoust. Soc. Am. 116 (2004) 1416–1426, doi: 10.1121/1.1780575.

28. W.J. Devenport, J.K. Staubs, S.A.L. Glegg, Sound radiation from real airfoils in turbulent flows, J. Acoust. Soc. Am. 116 (2004) 3498–3506. doi:10.1121/1.1788775.

29. S.A.L Glegg, W.J. Devenport, Panel methods for airfoils in turbulent flow, J. Sound Vib. 329 (2010) 3709–3720. doi:10.1016/j.jsv.2010.03.007.

30. F. Gea-Aguilera, J. Gill, X. Zhang, X. Chen, T. Node-Langlois, Leading edge noise predictions using anisotropic synthetic turbulence, 22nd AIAA/CEAS Aeroacoustics Conference, Lyon, France, 2016. doi:10.2514/6.2016-2840.

31. S. Zhong, X. Zhang, On the effect of streamwise disturbance on the airfoil-turbulence interaction noise, J. Acoust. Soc. Am. 145 (2019) 2530–2539. doi:10.1121/1.5098783.

32. Z. Shen, X. Zhang, Direct anisotropic filter method of generating synthetic turbulence applied to turbulence-airfoil interaction noise prediction, J. Sound Vib. 458 (2019) 544–564. doi:10.1016/j.jsv.2019.07.003.

33. F. Gea-Aguilera, J. Gill, X. Zhang, On the effects of fan wake modelling and vane design on cascade noise, J. Sound Vib. 459 (2019) 114859. doi:10.1016/j.jsv.2019.114859.

34. J.W. Kim, Optimised boundary compact finite difference schemes for computational aeroacoustics, J. Comput. Phys. 225 (2007) 995–1019. doi:10.1016/j.jcp.2007.01.008.

35. J.W. Kim, High-order compact filters with variable cut-off wavenumber and stable boundary treatment, Comput. Fluids 39 (2010) 1168–1182. doi:10.1016/j.compfluid.2010.02.007.

36. F.Q. Hu, M.Y. Hussaini, J.L. Manthey, Low-dissipation and low-dispersion Runge-Kutta schemes for computational acoustics, J. Comput. Phys. 124 (1996) 177–191. doi:10.1006/jcph.1996.0052.

37. J. Gill, R. Fattah, X. Zhang, Towards an effective non-reflective boundary condition for computational aeroacoustics, J. Sound Vib. 392 (2017) 217–231. doi:10.1016/j.jsv.2016.11.036.

38. V. Clair, C. Polacsek, T.L. Garrec, G. Reboux, M. Gruber, P. Joseph, Experimental and numerical investigation of turbulence-airfoil noise reduction using wavy leading edges, AIAA J. 51 (2013) 2695–2713. doi:10.2514/1.J052394.

39. J.W. Kim, S. Haeri, An advanced synthetic eddy method for the computation of aerofoil-turbulence interaction noise, J. Comput. Phys. 287 (2015) 1–17. doi:10.1016/j.jcp.2015.01.039.

40. R. Ewert, Broadband slat noise prediction based on CAA and stochastic sound sources from a fast random particle-mesh (RPM) method, J. Comput. Phys. 37 (2008) 369–387. doi:10.1016/j.compfluid.2007.02.003.

41. S.H. Huang, Q.S. Li, J.R. Wu, A general inflow turbulence generator for large eddy simulation, J. Wind Eng. Ind. Aerodyn. 98 (2010) 600–617. doi:10.1016/j.jweia.2010.06.002.

42. H.G. Castro, R.R. Paz, A time and space correlated turbulence synthesis method for large eddy simulations, J. Comput. Phys. 235 (2013) 742–763. doi:10.1016/j.jcp.2012.10.035.

43. A. Wohlbrandt, N. Hu, S. Guérin, R. Ewert, Analytical reconstruction of isotropic turbulence spectra based on the Gaussian transform, Comput. Fluids 132 (2016) 46–50, doi: 10.1016/j.compfluid.2016.03.023.

44. M. Dieste, G. Gabard, Random particle methods applied to broadband fan interaction noise, J. Comput. Phys. 231 (2012) 8133–8151, doi: 10.1016/j.jcp. 2012.07.044.

45. H.W. Liepmann, J. Laufer, K. Liepmann, On the spectrum of isotropic turbulence, NACA Tech. Rep., TN-2473, 1951.

46. Panel session: fan broadband noise predictions, 2014. web.laoal.org/Proceedings/NSF/FB-NWorkshop.nsf (Accessed 3 June 2019).

47. D.J. Thomson, Spectrum broadband estimation and harmonic analysis, Proc. IEEE 70 (1982) 1055–1062. doi:10.1109/PROC.1982.12423.

48. R. Fattah, D. Angland, X. Zhang, A priori grid quality estimation for high-order finite differencing, J. Comput. Phys. 315 (2016) 629–643. doi:10.1016/j.jcp.2016.03.063.

49. F. Farassat, G.P. Succi, The prediction of helicopter discrete frequency noise, Vertica 7 (1983) 309–320.

50. J. Gill, X. Zhang, P. Joseph, Symmetric airfoil geometry effects on leading edge noise, J. Acoust. Soc. Am. 134 (2013) 2669–2680. doi:10.1121/1.4818787.

51. T. Hainaut, G. Gabard, V. Clair, A CAA study of turbulence distortion in broadband fan interaction noise, 22nd AIAA/CEAS Aeroacoustics Conference, Lyon, France, 2016. doi:10.2514/6.2016-2839.

52. Z. Shen, X. Zhang, Distortion of anisotropic turbulence spectrum in the vicinity of aerofoil leading edge, Inter-Noise, Madrid, Spain, 2019.

53. R.K. Amiet, Compressibility effects in unsteady thin-airfoil theory, AIAA J. 12 (1974) 252–255. doi:10.2514/3.49212.

54. R.K. Amiet, High frequency thin-airfoil theory for subsonic flow, AIAA J. 14 (1976) 1076–1082. doi:10.2514/3.7187.